

Australian National University

ENGN4718

Engineering Research and Development Project

Rigid Body State Estimation From Sparse Range Measurements

Montiel Abello

2016

Supervised by Dr Jochen Trumpf and Dr Viorela Ila

Acknowledgements

Abstract

TEXT

Contents

Acknowledgments	i
Abstract	ii
Aims and Contributions	ix
1 Introduction	1
1.1 Literature Review	2
1.1.1 Infinite-Dimensional Observers	2
1.1.1.1 Linear Systems	2
1.1.1.2 Nonlinear Systems	3
1.1.2 Symmetry-Preserving Observers	4
1.1.2.1 Early work	4
1.1.2.2 Active Research	5
2 Theoretical Background	8
2.1 Rigid Body Kinematics	8
2.1.1 Lie Groups	8
2.1.1.1 Matrix Lie groups	9
2.1.1.2 Lie algebra	9
2.1.1.3 The exponential map and logarithm map	9
2.1.1.4 Infinitesimal generators	10
2.1.1.5 Lie bracket and group operation	11
2.1.1.6 Actions	11
2.1.2 $\text{SO}(3)$	11
2.1.2.1 Lie algebra	12
2.1.2.2 Actions	13

2.1.2.3	Rotation representations	13
2.1.2.4	Rotation matrices	13
2.1.2.5	Scaled-axis representation	13
2.1.2.6	Rotation quaternions	14
2.1.3	SE(3)	15
2.1.3.1	Lie algebra	15
2.1.3.2	Actions	16
2.1.4	Reference Frames	17
2.1.4.1	Pose	17
2.1.4.2	Point	18
2.1.4.3	Homogeneous coordinates	18
2.1.4.4	Redefining the reference frame of a point	18
2.1.4.5	Concatenating poses	19
2.1.4.6	Redefining the reference frame of a pose	19
2.1.4.7	Inverse	19
2.1.5	Rigid Body State Representation	19
2.1.6	Rigid Body Kinematics	20
2.1.7	Scanning Laser Range-finder Dynamic Model	20
2.2	State Observers	22
2.2.1	Luenberger observers	22
2.2.2	Symmetry-preserving observers	23
3	Problem Statement	24
3.1	Estimating the pose and size of a cube from sparse range measurements . .	25
3.2	Deliverables	28
4	Observer Simulation	29
4.1	Implementation	29
4.1.1	Rigid Body Motion	31
4.1.1.1	Interpolation	32
4.1.1.2	Numerical Integration	33
4.1.2	Sensor modelling: <code>initialisesensor</code>	34
4.1.2.1	Motion	34
4.1.2.2	Scanning	35

4.1.2.3	Hokuyo UBG-04LX-F01 Model	36
4.1.3	Environment Modelling: <code>initialiseenvironment</code>	37
4.1.3.1	Motion	37
4.1.3.2	Rigid Objects	38
4.1.4	Measurement Modelling	39
4.1.4.1	Range Computation: <code>computerange</code>	39
4.1.4.2	Sensor Noise: <code>addnoise</code>	41
4.1.5	Observer Implementation	41
4.1.5.1	Estimate: <code>estimatestate</code>	41
4.1.5.2	Object/background separation: <code>identifyobject</code>	43
4.1.5.3	Update: <code>updatestate</code>	43
4.2	Results	52
4.2.1	Orientation correction	52
4.2.1.1	Stationary Cube	52
4.2.1.2	Moving Cube	53
4.2.2	Position correction	54
4.2.3	Size correction	56
4.2.4	Orientation and size correction	57
4.2.5	Discussion	58
5	Experimental Data	61
5.1	Sensor Noise Characterisation	62
5.1.1	Measurement Setup	62
5.1.2	Results	63
5.1.2.1	Gaussian noise model	65
5.1.2.2	Surface noise	66
5.2	Observer Performance Testing Data	68
5.2.1	Setup	68
5.2.2	Results	69

List of Figures

1.1	Infinite dimensional optical flow discretised and computed in separate, independent regions	7
2.1	Transformations between reference frames $\{F\}$, $\{A\}$ and $\{B\}$ defined with respect to $\{F\}$	17
3.1	Range measurements of a cube from a depth sensor	25
4.1	Scanning behaviour of the UBG-04LX-F01 and parameters used to model it	37
4.2	Cube modelled with an ordered set of points and corresponding triangles .	39
4.3	Ray-triangle intersection	40
4.4	Orientation update scheme: intersection of the scan directions with the surfaces of the measured and predicted cubes are used to determine the surface normals.	45
4.5	Position update	48
4.6	Size update - case 1	50
4.7	Size update - case 2	51
4.8	Orientation update when single cube face visible leads to (a) angle error, depicted in final state estimate (b).	53
4.9	Angle error for (a) noiseless and (b) noisy measurements of stationary cube with 3 faces visible to sensor	54
4.10	Angle error when cube rotating with angular velocity of approximately 0.0327 rad/s such that 3 faces visible to sensor. Noiseless measurements used to update orientation via (a) screw matrix and (b) twist matrix. Noisy measurements used to update orientation via (c) screw matrix and (d) twist matrix.	54

4.11 Position error for stationary cube with single face visible to sensor. Position error (a) converges quickly for noiseless measurements when $p_{scale} = 0.01$. Position error (b) is unstable for noisy measurements if $p_{scale} = 0.01$. Position error (c) converges to noise floor for noisy measurements when $p_{scale} = 0.001$.	55
4.12 Position error for stationary cube with 2 faces visible to sensor	56
4.13 For noisy measurements of a stationary cube with 3 faces visible to the sensor, the size error ratio converges to the noise floor	56
4.14 For noisy measurements of a cube rotating at 0.0327 rad/s and translating at 0.0094 m/s such that 3 faces are visible to the sensor, the size error ratio converges to the noise floor	57
4.15 For noisy measurements of stationary cube with 3 faces visible to sensor, the angle error (a) and size error ratio (b) both converge to the noise floor.	57
4.16 Time taken to converge to (a) angle error $< \pi/400$ radians (1% of maximum $\pi/4$ angle error) and (b) size error ratio $< 0.01 $ for range of initial conditions	58
4.17 Noiseless measurements of cube rotating at 0.0327 rad/s such that 3 faces visible to sensor. Angle error (a) and size error ratio (b) when orientation updated via screw. Angle error (c) and size error ratio (d) when orientation updated via wrench.	59
4.18 Angle error (a) and size error ratio (b) for noiseless measurements of tetrahedron of side length $s = 0.5\text{m}$	60
5.1 setup to measure noise at a different ranges and angle (lights turned off during measurement to eliminate error from variation in lighting conditions)	62
5.2 Sensor noise function $f_{UBG}(r, \theta)$ approximately normally distributed	63
5.3 mean range error ($r_{error} = r_{groundtruth} - r_{measured}$) vs (r, θ) showing (a) large error at high angles and range, (b) overall shape	64
5.4 range error σ vs (r, θ) showing (a) outliers/large std dev at high angles and range, (b) overall shape	64
5.5 polynomials fitted to range error mean & standard deviation data points to model noise. (a) SSE: 0.003234, R-square: 0.8447, Adjusted R-square: 0.8278, RMSE: 0.005027(b) SSE: 7.592e-06, R-square: 0.9196, Adjusted R-square: 0.9103, RMSE: 0.0002515	65

5.6 Comparision of (a) measured and (b) simulated surface noise. Point distribution along radial lines is shown as quintiles of error.	67
5.7 setup to collect experimental data	68

Aims and Contributions

Aims: start new research, exploratory

Outcomes: -observer design

-simulation toolbox for scanning laser range-finder and rigid bodies. -noise model for Hokuyo UBG-04LX-F01 - more complete model (combines effect of range, angle) in conditions tested than existing literature Contributions: used Viorela's functions for conversions between rotation representations. Used aerospace toolbox functions for quaternion stuff.

Did everything else

Chapter 1

Introduction

CONTEXT

autonomous robots, unstructured environments. Advances in hardware - need improvements in software to fully utilise capabilities of dense sensors. What is needed is observer design methodology. MOTIVATION

Allow for improved convergence, global. RESEARCH GOALS

Exploratory, look into sparse sensor - dense measurements. Build an observer for an infinite dimensional system - in this case, simplified at first. Will explore if infinite dimensional, symmetry preserving implementation would improve performance

WHAT IS IN REPORT
This report presents the implementation of an observer to solve a novel problem: estimating
Simulation - to test performance, experimental validation

implementation of an observer to solve novel problem - sparse sensor gives dense measurement. Sparse measurements from a range sensor dense measurement part of new direction of research into infinite dimensional symmetry preserving observers. Section 1.1 reviews literature infinite dimensional observers. Looks at methods for design. Relevant background for ... symmetry, state representation. Lie groups. Present problem - detailed breakdown, how it fits into lit. Detailed description of simulation implementation including observer update function design. Chapter experimental data - noise model + measurements collected

1.1 Literature Review

The use of dense sensors allows for a more accurate estimation of the state of an infinite-dimensional system such as a complex, real-world environment. The theory of infinite-dimensional observers is required to fully utilise this information. This section will review the current state of design methodologies and implementations for infinite-dimensional observers. Particular focus will be paid to an emerging avenue of research; symmetry-preserving observer design. Recent theory developments in this area have allowed limitations in the global convergence properties of infinite-dimensional observers to be overcome.

1.1.1 Infinite-Dimensional Observers

In many real world systems the dependent variables are functions of one or more spatial variables. An example would be the dynamics of waves in a body of water. The height of the surface varies continuously along the x and y directions. These spatial variables vary continuously, meaning an infinite number of parameters is required to describe the state of the system. Such systems are termed *infinite-dimensional systems*, or *distributed parameter systems*. Their dynamics are modelled by a partial differential equation (PDE).

When a state estimate is required but direct measurement of the state with sensors is difficult or impossible, a *state observer* is employed. A state observer is a filter that provides an estimate of the state of a system using the difference between its measured and predicted outputs. A more detailed description of an observer is provided in section 2.2. An observer for an infinite-dimensional system is called an *infinite-dimensional observer*.

1.1.1.1 Linear Systems

Observer theory for *linear* infinite-dimensional systems has been widely studied. The techniques used are typically extensions of Luenberger observers and Kalman filter methods used to observe finite dimensional systems.

A simplified approach is to use a spatial discretisation method such as finite difference or finite element to reduce the infinite-dimensional system to a finite-dimensional one. From here, finite-dimensional observer design techniques can be used. This is known as the

early lumping method, and was employed by Stavroulakis [1] who implemented a finite-dimensional observer as part of a control system for an infinite dimensional systems.

The early lumping approach suffers from *spillover*, a phenomenon where performance is affected by the neglected dynamics of the system[2]. Harkort [3] recently developed an observer based control scheme that reduced this effect by using modelled outputs rather than true measurements to reduce the effect of the neglected dynamics.

More accurate observers can be designed with the *late lumping* approach which uses the infinite-dimensional model of the system in the observer design. The result is an infinite-dimensional observer that is discretised later for practical implementation. These methods are typically extensions of Kalman or Luenberger methods to infinite dimensions.

Early work by Gressang [4] extended the Luenberger observer to infinite-dimensional systems whose state space was an abstract Banach space whose dynamics were defined by an infinitesimal generator of a semigroup. More recently, Smyshlyaev [5] developed an exponentially converging backstepping observer for systems governed by parabolic PDEs. Ramdani introduced forward and backward observers [6] whose convergence properties were investigated by Haine [7].

1.1.1.2 Nonlinear Systems

There is currently no universal approach for observer design for nonlinear infinite-dimensional systems. The most common approach has been to linearise the system, then apply a linear infinite-dimensional observer design. Common linearisation methods are Lyapunov methods, extended linearisation and the Lie-algebraic approach [8].

There has been some progress in infinite-dimensional observer design for special cases of nonlinear systems. For bilinear systems, Xu [9] designed an infinite-dimensional observer that converged for certain inputs. Bounit [10] designed Kalman and Luenberger type observers for infinite-dimensional bilinear systems.

Despite these small advances in special case nonlinear design, the most common design methods for nonlinear infinite-dimensional systems rely on linearisation techniques. These techniques rely on the fact that differentiable functions can be approximated by a first-order Taylor expansion around a point. Luenberger and Kalman methods can be applied to linear approximations of system infinite-dimensional systems around an equilibrium point.

This simplification relies on the dynamics of system at the point of linearisation being representative of the entire space. In general, this is not necessarily true, and is the biggest limitation in this design technique. The result is that these linearised observers only converge if the initial state estimate is within a local neighbourhood of the true state. Global converge is not guaranteed which severely limits robustness.

Global convergence can be achieved by taking account the symmetries inherent to the system during observer design. A powerful tool for dealing with symmetries is the theory of *Lie groups*. Investigation into *symmetry-preserving* observer design for systems on Lie groups is an active area of research. It promises to produce theoretically validated design principles for nonlinear infinite-dimensional observers, though the majority of research so far has been limited to finite-dimensional observers.

1.1.2 Symmetry-Preserving Observers

The motivation behind symmetry-preserving observers is to take advantage of invariances in the dynamics of the system. The goal is to design an observer around an equilibrium point in such a way that it can be extended converge around a wider set of points.

1.1.2.1 Early work

Geometry conscious observer design is not a new idea. Early investigation by Marcus [11] into algebraic and geometric methods for nonlinear filter design showed promise. A seminal work by Salcudean [12] was the design of an eventually exponential, globally converging observer for the attitude of rigid bodies from orientation and torque measurements. This observer design takes advantage of the simplicity of the quaternion rotation representation and dynamics of rigid body motion.

Another important result that is a precursor to the active research of today is a design method developed by Aghannan & Rouchon [13]. Their invariant observer construction was based on Cartan's moving frame method. Though convergence was proven for a specific problem, the observer convergence for a general case was left an open problem. Maithripala [14] demonstrated the effectiveness of Aghannan & Rouchons' method by incorporating it into the design of an intrinsic observer based controller. Performance was shown to be independent of the coordinate system used to represent the configuration space.

1.1.2.2 Active Research

There are currently two groups actively researching symmetry-preserving observer design. Both have begun to apply symmetry-preserving methods to infinite-dimensional observers.

The work of Bonnabel, Auroux, Rouchon, Martin et al. is a progression of the early results from Aghannan & Rouchon. Their general approach is to first design a Luenberger type observer around an equilibrium point. An invariant frame is used to construct an invariant output error. The observer innovation term respects the symmetries of the system and thus the nonlinear observer is well behaved around a continuum of equilibrium points.

In [15], a design procedure was developed, based on Aghannan & Rouchons' work. Asymptotic stability was achieved, though this required a design procedure tailored to specific nonlinearities of the system and did not apply in a general case. It was shown in [16] that the invariant error equation simplified convergence analysis. The observer's global behaviour improved, having a larger region of attraction in comparison to naively linearised observers. Developments were made to the theory and presented in [17]. For a particular class of invariant system it was shown that the observer converged locally around any trajectory, and global convergence behaviour was independent of trajectory.

Most recently [18], these invariant design methods were applied to an infinite dimensional system. An observer estimating the state of fluid in a water tank where height varies with continuous dependent variables position and time was developed. It was shown to converge more quickly and robustly than previous attempts at infinite dimensional observer designed with Extended Kalman Filter (EKF) methods.

The work of Trumper, Mahony, Hamel, Lageman et al. differs in scope. The methods of Bonnabel et al. are generalised and can be applied to a wide range of systems. In contrast, the work of Trumper et al. is limited to two specific classes of systems, but achieves stronger convergence properties. In [19] nonlinear filters on the Special Orthogonal Group **SO**(3) are used in attitude estimation and the resulting nonlinear observers achieved almost globally stable observer error. Another attitude observer [20] achieved almost globally asymptotic and locally exponential convergence. In [21], the design methodology for 2 classes of systems is presented. The approach taken is to lift the kinematic system onto its symmetry group and design an observer for the lifted system. The Lyapunov method

is used to design the observer innovation term. This methodology simplifies nonlinear observer design and produces observers with strong convergence properties. This group has also begun research on symmetry-preserving infinite-dimensional observers.

The motivation behind the development of infinite-dimensional observers is to allow dense sensors to be fully utilised. In this vein, research presented in a PhD thesis by Zarrouati [22] utilised dense measurements from a camera and depth sensor. An observer was developed from rotation invariant equations for light and depth. Though the sensors took measurements of an infinite dimensional state, a finite dimensional approximation of this state is what was estimated by the observer.

Another recent work by Adarve et al.[23] also uses dense sensing in the estimation of an infinite dimensional state. This result will be examined closely as it is similar in direction to this research.

Adarve et al. design an update-propagation filter to iteratively compute dense optical flow Φ from CCD camera measurements Y . This optical flow is an infinite dimensional state. Rather than computing the optical flow independently at each frame, a two-stage process is used to build it incrementally. The propagation stage uses a non-linear PDE to model the transport of the optical flow in the next time step. The update stage corrects this prediction using the current image.

The iterative filter used in this approach is an observer that estimates the state of the continuous spatio-temporal flow field. By using a dense sensor, the measured image stream can be treated as a continuous, infinite dimensional state. This is in contrast to sparse optical flow computation where the image is modelled as a set of discrete pixel values. However, the flow fields Φ discretised and computed in r in independent regions Ω around a discrete set of control points ξ as shown in Figure 1.1.2.2. Here, this approach differs from that of general infinite dimensional invariant observer. The state is treated as a discrete set of locally continuous states which does not allow for symmetry considerations. This is because the PDE relations in the local regions are invariant to 2D rotation and translation, but the interactions between regions themselves are not.

Discretising Φ and Y at the beginning of the algorithm design means this is an early lumping design approach. Employing a late lumping approach by discretising an infinite dimensional observer would allow the for the rotation and translation invariance of the flow field to be taken advantage of to improve convergence properties.

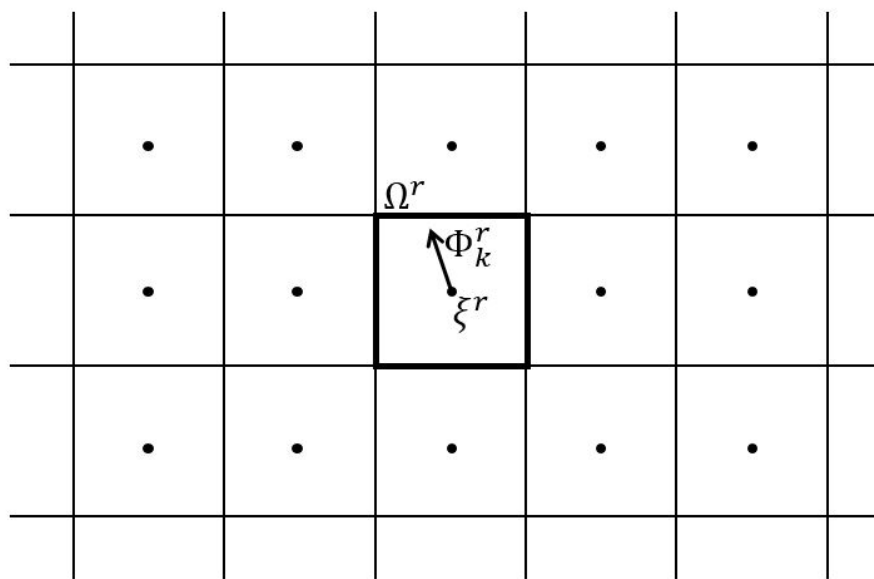


Figure 1.1: Infinite dimensional optical flow discretised and computed in separate, independent regions

The lesson to take from this analysis is that discretisation methods must be carefully chosen in order to preserve the invariance of the system.

Chapter 2

Theoretical Background

2.1 Rigid Body Kinematics

A rigid body is a model of a solid object whose deformation is assumed to be negligible. The distance between every pair of points on the body remains constant. Because such a body does not deform, knowledge of the orientation and position of a reference frame fixed to a rigid body constitutes knowledge of the position of all points. The position of the rigid body is thus defined by the position of a particular point in the body, most commonly its centre of mass. The orientation can be defined using a set of coordinate axes fixed to the body such that its origin coincides with the position point. The theory of Lie groups will be used to describe the kinematics of rigid bodies in this report.

2.1.1 Lie Groups

A Lie group \mathbf{G} is a group whose elements form a differentiable manifold and whose group operation and inverse operation are differentiable. As a group, \mathbf{G} is a set of elements and a group operation. This group operation is a binary operation that combines two elements and is denoted by multiplication: AB or $A \cdot B$ for $A, B \in \mathbf{G}$. Because it is a group, \mathbf{G} satisfies the 4 group axioms:

- **Closure:** The group operation $\mathbf{G} \times \mathbf{G} \mapsto \mathbf{G}$ is a function that maps elements of \mathbf{G} onto itself; $\forall A, B \in \mathbf{G}, AB \in \mathbf{G}$.
- **Associativity:** Elements of \mathbf{G} are associative under the group operation; $\forall A, B, C \in$

\mathbf{G} , $(AB)C = A(BC)$.

- **Identity:** There exists an identity element $I \in \mathbf{G}$ such that $\forall A \in \mathbf{G}$, $IA = AI = A$.
- **Inverse:** For all $A \in \mathbf{G}$ there exists an inverse element $A^{-1} \in \mathbf{G}$ such that $AA^{-1} = A^{-1}A = I$.

Because the Lie group \mathbf{G} is a differentiable manifold, it is locally Euclidean. This means that the neighbourhood around every element of \mathbf{G} can be approximated with a tangent plane. This property allows calculus to be performed on elements of \mathbf{G} .

2.1.1.1 Matrix Lie groups

A matrix Lie group $\mathbf{G} \subset \mathbf{GL}(n)$ is made up of group elements which are $n \times n$ matrices. This work will focus on matrix Lie groups because the form of the exponential map and Lie bracket functions provided below only apply to such Lie groups. Generalised concepts for these functions exist, but a more detailed and relevant description can be given by focusing on matrix Lie groups.

2.1.1.2 Lie algebra

The tangent space at the identity element of a Lie group is called the Lie algebra \mathfrak{g} . It is called the Lie *algebra* because it has a binary operation, known as the Lie bracket $[X, Y]$. For matrix Lie groups the Lie bracket is

$$[A, B] \stackrel{\Delta}{=} AB - BA \quad (2.1)$$

2.1.1.3 The exponential map and logarithm map

The canonical mapping from the Lie algebra \mathfrak{g} to the Lie group \mathbf{G} is called the exponential map:

$$\exp : \mathfrak{g} \rightarrow \mathbf{G} \quad (2.2)$$

Similarly, the logarithm map maps elements from its domain $\mathbf{D} \subset \mathbf{G}$ to \mathfrak{g}

$$\log : \mathbf{D} \rightarrow \mathfrak{g} \quad (2.3)$$

such that for a group element A ,

$$\exp(\log(A)) = A \quad (2.4)$$

For matrix Lie groups, the exponential map and logarithm map correspond to the matrix exponential and matrix logarithm respectively.

2.1.1.4 Infinitesimal generators

The *hat* operator $(\cdot)^\wedge$ can be used to map an n -vector to an $m \times m$ matrix representation, when $\mathbb{R}^{m \times m}$ is isomorphic to \mathbb{R}^n .

$$\begin{aligned} (\cdot)^\wedge : \mathbb{R}^n &\rightarrow \mathbb{R}^{m \times m} \\ x \mapsto x^\wedge &= \sum_{i=1}^n x_i G_i \end{aligned} \quad (2.5)$$

where the set of elements G_i form a basis for $\mathbb{R}^{m \times m}$.

Conversely, the *vee* operator $(\cdot)^\vee$ maps matrices in $\mathbb{R}^{m \times m}$ to vectors in \mathbb{R}^n such that $(x^\wedge)^\vee = x$

$$\begin{aligned} (\cdot)^\vee : \mathbb{R}^{m \times m} &\rightarrow \mathbb{R}^n \\ x^\wedge \mapsto x & \end{aligned} \quad (2.6)$$

For an n -dimensional matrix Lie group, the Lie algebra \mathfrak{g} is a vector space isomorphic to \mathbb{R}^n . The hat operator $(\cdot)^\wedge$ maps vectors $x \in \mathbb{R}^n$ to elements of \mathfrak{g} . For a matrix Lie group \mathbf{G} whose elements are $m \times m$ matrices, the elements of \mathfrak{g} will also be $m \times m$ matrices.

$$\begin{aligned} (\cdot)^\wedge : \mathbb{R}^n &\rightarrow \mathfrak{g} \\ x \mapsto x^\wedge &= \sum_{i=1}^n x_i G_i \end{aligned} \quad (2.7)$$

The basis elements G_i are $m \times m$ matrices known as the infinitesimal generators of \mathbf{G} .

2.1.1.5 Lie bracket and group operation

For Lie groups endowed with the commutative property ($\forall A, B \in \mathbf{G}, AB = BA$), vector addition in the Lie algebra maps to a group operation in the Lie group. For $C = A + B$ where $A, B, C \in \mathfrak{g}$,

$$e^C = e^{A+B} = e^A e^B \quad (2.8)$$

For non-commutative Lie groups, this relationship between the Lie algebra and Lie group operations do not hold. Instead, for $C = \log(e^A e^B)$, C is calculated with the Baker-Campbell-Hausdorff formula:

$$C = A + B + \frac{1}{2}[A, B] + \frac{1}{12}[A - B, [A, B]]\frac{1}{24}[B, [A, [A, B]]] + \dots \quad (2.9)$$

2.1.1.6 Actions

When a group action for a Lie group \mathbf{G} acting on a manifold M is a differentiable map, this is known as a Lie group action. For example, 3D rotations act on 3D points so the Lie group $\mathbf{SO}(3)$ acts on \mathbb{R}^3 . A left action of \mathbf{G} on M is defined as a differentiable map

$$\Phi : \mathbf{G} \times M \mapsto M \quad (2.10)$$

where

- the identity element I acts as the identity on M

$$\Phi(I, m) = m \quad \forall m \in M \quad (2.11)$$

- Group actions compose according to

$$\Phi(m, \Phi(n, o)) = \Phi(mn, o) \quad \forall m, n, o \in M \quad (2.12)$$

2.1.2 $\mathbf{SO}(3)$

A rotation represents the motion of a point about the origin of a Euclidean space. In \mathbb{R}^3 this is a proper isometry: a transformation that preserves distances between any pair of points and has a determinant of +1. The set of all rotations about the origin of \mathbb{R}^3 is

known as the *special orthogonal group* $\mathbf{SO}(3)$. Group elements of $\mathbf{SO}(3)$ can be represented using a special subset of 3×3 invertible matrices and in this case, forms a matrix Lie group. Several rotation representations are described later in this section, but the theory presented below only applies to matrix Lie groups which rely on the rotation matrix representation for group elements.

A rotation matrix \mathbf{R} is a 3×3 matrix that performs a rotation operation when it acts on an element of \mathbb{R}^3 . The properties of \mathbf{R} are described in more detail below.

2.1.2.1 Lie algebra

The Lie algebra $\mathfrak{so}(3)$ is a vector space whose elements represent angular velocities. These elements can be represented with 3×3 skew-symmetric matrices $\boldsymbol{\omega}^\wedge$, where $\boldsymbol{\omega} \in \mathbb{R}^3$ is a 3-vector representing an angular velocity. For $\boldsymbol{\omega} = [\omega_1 \ \omega_2 \ \omega_3]^T$, the skew symmetric representation is given by taking the hat representation of $\boldsymbol{\omega}$

$$\boldsymbol{\omega}^\wedge = \begin{bmatrix} 0 & -\omega_3 & \omega_2 \\ \omega_3 & 0 & -\omega_1 \\ -\omega_2 & \omega_1 & 0 \end{bmatrix} \quad (2.13)$$

Elements of $\mathfrak{so}(3)$ are mapped to $\mathbf{SO}(3)$ according to the exponential map:

$$\begin{aligned} \exp : \mathfrak{so}(3) &\rightarrow \mathbf{SO}(3) \\ \boldsymbol{\omega}^\wedge &\mapsto \exp(\boldsymbol{\omega}^\wedge) \end{aligned} \quad (2.14)$$

where the matrix $\exp(\boldsymbol{\omega}^\wedge) \in \mathbf{SO}(3)$ is a rotation matrix \mathbf{R} .

Conversely, the logarithm map maps 3×3 rotation matrices of $\mathbf{SO}(3)$ to elements of $\mathfrak{so}(3)$:

$$\begin{aligned} \log : \mathbf{SO}(3) &\rightarrow \mathfrak{so}(3) \\ \exp(\boldsymbol{\omega}^\wedge) &\mapsto \boldsymbol{\omega}^\wedge \end{aligned} \quad (2.15)$$

This means that for a rotation matrix \mathbf{R} , $\log(\mathbf{R}) \in \mathfrak{so}(3)$ and represents an angular velocity.

2.1.2.2 Actions

By the group action, elements of $\mathbf{SO}(3)$ rotate points $\mathbf{p} \in \mathbb{R}^3$ about the origin.

$$\begin{aligned}\Phi : \mathbf{SO}(3) \times \mathbb{R}^3 &\rightarrow \mathbb{R}^3 \\ (\mathbf{R}, \mathbf{p}) &\mapsto \mathbf{Rp}\end{aligned}\tag{2.16}$$

2.1.2.3 Rotation representations

There are many conventions by which elements of $\mathbf{SO}(3)$ can be represented. The representations that will be used in this report are described below.

2.1.2.4 Rotation matrices

A 3D rotation matrix \mathbf{R} is an orthogonal 3×3 matrix with a determinant of +1. Since \mathbf{R} is orthogonal, its columns and rows are respectively sets of orthogonal unit vectors and

$$\mathbf{R}^{-1} = \mathbf{R}^T\tag{2.17}$$

The group operation using rotation matrices is simply a matrix multiplication which concatenates the two rotations. The product of two rotation matrices $\mathbf{R}_3 = \mathbf{R}_2\mathbf{R}_1$ is a rotation matrix corresponding to left multiplication by \mathbf{R}_1 followed by \mathbf{R}_2 .

The left action of a rotation matrix \mathbf{R} on a point $\mathbf{p} \in \mathbb{R}^3$ is a left matrix multiplication that rotates \mathbf{p} about the origin.

2.1.2.5 Scaled-axis representation

An orientation in \mathbb{R}^3 can also be represented by a 3-vector $\boldsymbol{\theta}$ whose direction \mathbf{r} represents the axis of rotation and magnitude θ represents the angle of rotation.

$$\boldsymbol{\theta} = \theta\mathbf{r}\tag{2.18}$$

Though scaled-axis vectors are not typically used to perform rotations, Rodrigues' rotation

formula efficiently converts scaled-axis vectors to rotation matrices:

$$\mathbf{R}_\theta = \mathbf{I} + [\mathbf{r}]_\times \sin \theta + ([\mathbf{r}]_\times)^2 (1 - \cos \theta) \quad (2.19)$$

Elements of $\mathfrak{so}(3)$ are typically represented with the hat representation $\boldsymbol{\omega}^\wedge$ of a scaled-axis vector $\boldsymbol{\omega}$, where the magnitude $|\boldsymbol{\omega}|$ corresponds to the angular velocity about the axis $\boldsymbol{\omega}/|\boldsymbol{\omega}|$.

2.1.2.6 Rotation quaternions

Quaternions are an extension of complex numbers. The set of unit quaternions can be used to represent $\mathbf{SO}(3)$, and will be referred to as the set of rotation quaternions. A rotation quaternion \mathbf{q} is a 4-tuple of real numbers that encode the same information as the scaled-axis representation. \mathbf{q} is often described in terms of its first element w - the scalar part, and the remaining elements x, y and z - the vector part. Given an axis of rotation \mathbf{r} and an angle of rotation θ :

$$\mathbf{q} = \begin{bmatrix} w \\ x \\ y \\ z \end{bmatrix} = \begin{bmatrix} w \\ \mathbf{v} \end{bmatrix} = \begin{bmatrix} \cos(\theta/2) \\ \sin(\theta/2)\mathbf{r} \end{bmatrix} \quad (2.20)$$

In general, the quaternion inverse is given by

$$\mathbf{q}^{-1} = \frac{1}{w^2 + x^2 + y^2 + z^2} \begin{bmatrix} w \\ -x \\ -y \\ -z \end{bmatrix} \quad (2.21)$$

For unit magnitude rotation quaternions the inverse represents a rotation by $-\theta$ and is given by

$$\mathbf{q}^{-1} = \begin{bmatrix} \cos(\theta/2) \\ -\sin(\theta/2)\mathbf{r} \end{bmatrix} = \begin{bmatrix} w \\ -x \\ -y \\ -z \end{bmatrix} \quad (2.22)$$

The group operation is performed with quaternion multiplication which is defined:

$$\mathbf{q}_1 \mathbf{q}_2 = \begin{bmatrix} w_1 \\ \mathbf{v}_1 \end{bmatrix} \cdot \begin{bmatrix} w_2 \\ \mathbf{v}_2 \end{bmatrix} = \begin{bmatrix} w_1 w_2 - \mathbf{v}_1 \cdot \mathbf{v}_2 \\ w_1 \mathbf{v}_2 + w_2 \mathbf{v}_1 + \mathbf{v}_1 \times \mathbf{v}_2 \end{bmatrix} \quad (2.23)$$

As with rotation matrices, quaternion multiplication is associative but not commutative.

The group action rotates a point $\mathbf{p}_0 \in \mathbb{R}^3$ to $\mathbf{p}_1 \in \mathbb{R}^3$ by embedding it as the vector component of a quaternion and applying a conjugation operation with \mathbf{q} . The rotated vector \mathbf{p}_1 can be extracted as the vector component of the resulting quaternion.

$$\begin{bmatrix} 0 \\ \mathbf{p}_1 \end{bmatrix} = \mathbf{q} \begin{bmatrix} 0 \\ \mathbf{p}_0 \end{bmatrix} \mathbf{q}^{-1} \quad (2.24)$$

2.1.3 SE(3)

The special Euclidean group **SE**(3) represents rigid transformation in \mathbb{R}^3 . This is a matrix Lie group whose elements comprise the set of all rigid transformations in \mathbb{R}^3 and can be represented with 4×4 matrices of the form

$$\mathbf{S} = \begin{bmatrix} \mathbf{R} & \mathbf{p} \\ \mathbf{0}_{1 \times 3} & 1 \end{bmatrix} \quad (2.25)$$

where $\mathbf{R} \in \mathbf{SO}(3)$ and $\mathbf{p} = [p_x \ p_y \ p_z]^\top \in \mathbb{R}^3$.

SE(3) is a semidirect product of **SO**(3) and \mathbb{R}^3 . As its group elements contain a rotation matrix and translation vector, **SE**(3) has 6 degrees of freedom and is a 6-dimensional manifold.

2.1.3.1 Lie algebra

The Lie algebra **se**(3) is a vector space whose elements are 4×4 matrices of the form

$$\begin{bmatrix} \boldsymbol{\omega}^\wedge & \mathbf{v} \\ \mathbf{0}_{1 \times 3} & 0 \end{bmatrix} \quad (2.26)$$

where $\boldsymbol{\omega} = [\omega_x \ \omega_y \ \omega_z]^\top \in \mathbf{so}(3)$, representing an angular velocity in scaled axis representation, and $\mathbf{v} = [v_x \ v_y \ v_z]^\top \in T\mathbb{R}^3 \equiv \mathbb{R}^3$, representing a linear velocity vector.

Elements of $\mathfrak{se}(3)$ are mapped to $\mathbf{SE}(3)$ according to the exponential map:

$$\begin{aligned} \exp : \mathfrak{se}(3) &\rightarrow \mathbf{SE}(3) \\ \begin{bmatrix} \boldsymbol{\omega}^\wedge & \mathbf{v} \\ \mathbf{0}_{1 \times 3} & 0 \end{bmatrix} &\mapsto \begin{bmatrix} \mathbf{R} & \mathbf{p} \\ \mathbf{0}_{1 \times 3} & 1 \end{bmatrix} \end{aligned} \quad (2.27)$$

i.e. $\forall \mathbf{T} \in \mathfrak{se}(3)$, $\exp(\mathbf{T}) \in \mathbf{SE}(3)$

Conversely, the logarithm map maps elements of $\mathbf{SE}(3)$ to elements of $\mathfrak{se}(3)$:

$$\begin{aligned} \log : \mathbf{SE}(3) &\rightarrow \mathfrak{se}(3) \\ \begin{bmatrix} \mathbf{R} & \mathbf{p} \\ \mathbf{0}_{1 \times 3} & 1 \end{bmatrix} &\mapsto \begin{bmatrix} \boldsymbol{\omega}^\wedge & \mathbf{v} \\ \mathbf{0}_{1 \times 3} & 0 \end{bmatrix} \end{aligned} \quad (2.28)$$

i.e. $\forall \mathbf{S} \in \mathbf{SE}(3)$, $\log(\mathbf{S}) \in \mathfrak{se}(3)$

2.1.3.2 Actions

$\mathbf{SE}(3)$ group elements acts to perform a rigid transformation on points in \mathbb{R}^3 . This corresponds to a rotation about the origin and a translation. To apply a transformation using the 4×4 matrix elements of $\mathbf{SE}(3)$ to a point $\mathbf{p} = (x, y, z)$ in \mathbb{R}^3 , the point must be represented with homogeneous coordinates as \mathbf{p}'

$$\mathbf{p}' = \begin{bmatrix} \mathbf{p} \\ 1 \end{bmatrix} = \begin{bmatrix} x \\ y \\ z \\ 1 \end{bmatrix} \quad (2.29)$$

The left group action of $\mathbf{SE}(3)$ is now simply a left matrix multiplication of \mathbf{p} :

$$\mathbf{p}'_1 = \mathbf{S}\mathbf{p}'_0 = \begin{bmatrix} \mathbf{R} & \mathbf{p} \\ \mathbf{0}_{1 \times 3} & 1 \end{bmatrix} \begin{bmatrix} \mathbf{p}_0 \\ 1 \end{bmatrix} = \begin{bmatrix} \mathbf{R}\mathbf{p}_0 + \mathbf{p} \\ 1 \end{bmatrix} \quad (2.30)$$

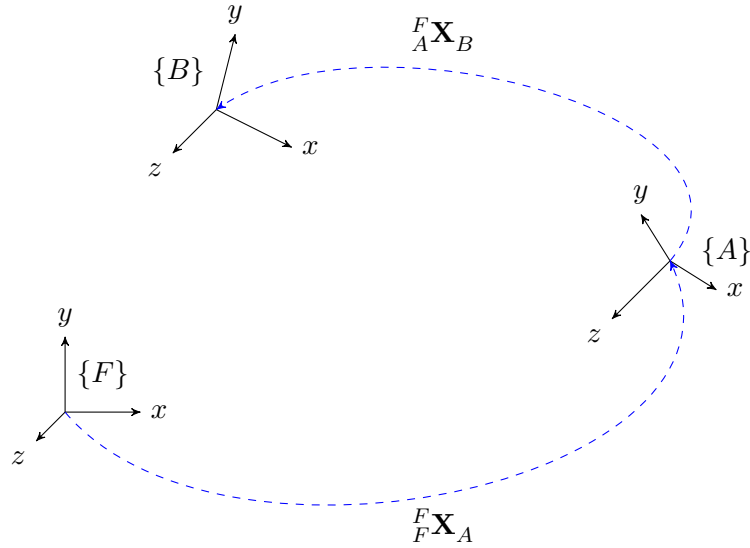


Figure 2.1: Transformations between reference frames $\{F\}$, $\{A\}$ and $\{B\}$ defined with respect to $\{F\}$

2.1.4 Reference Frames

A reference frame is a system of coordinates that is used to uniquely identify points on a manifold. This report will deal with reference frames on \mathbb{R}^3 , that are used both to define the position of a point and the pose of a rigid body in 3D space. Such a reference frame is represented by an element of $\text{SE}(3)$.

The notion of an inertial reference frame is introduced here. This will be defined as a reference frame that is stationary for the purpose of the problem being described. The convention used will be to denote the inertial reference frame as $\{F\}$.

Consider the three reference frames shown in Figure 2.1, denoted $\{F\}$ (the inertial frame), $\{A\}$ and $\{B\}$. The notation ${}_A\mathbf{X}_B$ defines the transformation in \mathbf{X} of the reference frame $\{B\}$ with respect to the frame $\{A\}$, defined in the frame $\{F\}$.

For example, ${}_A\mathbf{R}_B$ defines the rotation of $\{B\}$ with respect to $\{A\}$, defined in the inertial frame $\{F\}$.

2.1.4.1 Pose

A pose defines an orientation and position in space. The pose of a rigid body is represented by a reference frame fixed to a particular point within the body. The pose of the rigid body

with respect to another reference frame is defined by the relative position and orientation of the two frames. This transformation can be defined with respect to either reference frame and is represented by an element of $\mathbf{SE}(3)$. If a rigid body has orientation aligned with a reference frame $\{B\}$ and position at the origin of $\{B\}$, then the pose of the rigid body with respect to $\{A\}$ and defined in $\{F\}$ is:

$${}^F_A \mathbf{S}_B = \begin{bmatrix} {}^F_A \mathbf{R}_B & {}^F_A \mathbf{p}_B \\ \mathbf{0}_{1 \times 3} & 1 \end{bmatrix} \quad (2.31)$$

2.1.4.2 Point

A point $\mathbf{p} \in \mathbb{R}^3$ in the frame $\{F\}$ is denoted ${}^F \mathbf{p}$ and is expressed as a 3-vector of the weights used to compose it from the basis vectors of $\{F\}$.

$${}^F \mathbf{p} = \begin{bmatrix} {}^F x \\ {}^F y \\ {}^F z \end{bmatrix} \quad (2.32)$$

2.1.4.3 Homogeneous coordinates

To be acted on by an element of $\mathbf{SE}(3)$, a point must be expressed in homogeneous coordinates.

$${}^F \mathbf{p}' = \begin{bmatrix} {}^F \mathbf{p} \\ 1 \end{bmatrix} \quad (2.33)$$

2.1.4.4 Redefining the reference frame of a point

Consider a point in \mathbb{R}^3 defined as the position of the frame $\{A\}$ with respect to the frame $\{F\}$, defined in terms of the frame $\{A\}$. To redefine the point in terms of $\{F\}$, the left action of ${}^F \mathbf{S}_A \in \mathbf{SE}(3)$ is used:

$${}^F \mathbf{p}' = {}^F \mathbf{S}_A {}^A \mathbf{p}' \quad (2.34)$$

2.1.4.5 Concatenating poses

Poses are concatenated by multiplying relative poses.

$${}^F \mathbf{X}_B = {}^F \mathbf{X}_A {}^A \mathbf{X}_B \quad (2.35)$$

2.1.4.6 Redefining the reference frame of a pose

To define a pose transformation matrix in terms of a different reference frame, a matrix conjugation is used.

$${}^A \mathbf{X}_C = ({}^A \mathbf{X}_F) {}^F \mathbf{X}_C ({}^A \mathbf{X}_F)^{-1} \quad (2.36)$$

2.1.4.7 Inverse

Taking the inverse of a pose transformation matrix has the effect of reversing the transformation, but does not alter the frame that the transformation is defined in terms of.

$$({}^A \mathbf{X}_B)^{-1} = {}^B \mathbf{X}_A \quad (2.37)$$

2.1.5 Rigid Body State Representation

The state of a rigid body moving through 3D space can be represented by its linear and angular position, velocity and acceleration. Higher derivatives could be taken but will be ignored for simplicity. The inertial frame is denoted $\{F\}$ and a frame $\{A\}$ is fixed to the pose of the moving body.

The pose of the body with respect to the inertial frame at time t , defined in $\{F\}$ is represented by the **screw** matrix ${}^F \mathbf{S}_A(t) \in \mathbf{SE}(3)$,

$${}^F \mathbf{S}_A(t) = \begin{bmatrix} {}^F \mathbf{R}_A(t) & {}^F \mathbf{p}_A(t) \\ \mathbf{0}_{1 \times 3} & 1 \end{bmatrix} \quad (2.38)$$

where ${}^F \mathbf{R}_A(t) \in \mathbf{SO}(3)$ is a rotation matrix, and ${}^F \mathbf{p}_A(t) \in \mathbb{R}^3$ represents the position of the body defined in $\{F\}$.

The linear and angular velocity of the body at time t with respect to $\{F\}$, defined in the

body-fixed frame $\{A\}$ is represented by the **twist** matrix ${}_F^A \mathbf{T}_A(t) \in \mathfrak{se}(3)$,

$${}_F^A \mathbf{T}_A(t) = \begin{bmatrix} {}_F^A \boldsymbol{\omega}_A^\wedge(t) & {}_F^A \mathbf{v}_A(t) \\ \mathbf{0}_{1 \times 3} & 0 \end{bmatrix} \quad (2.39)$$

where ${}_F^A \boldsymbol{\omega}_A(t) \in \mathfrak{so}(3)$ is an angular velocity in the scaled-axis representation, and the linear velocity is ${}_F^A \mathbf{v}_A(t) \in T\mathbb{R}^3 \equiv \mathbb{R}^3$.

The linear and angular acceleration of the body at time t with respect to $\{F\}$, defined in the body-fixed frame $\{A\}$, is represented by the **wrench** matrix ${}_F^A \mathbf{W}_A(t) \in T\mathfrak{se}(3) \equiv \mathfrak{se}(3)$,

$${}_F^A \mathbf{W}_A(t) = \begin{bmatrix} {}_F^A \boldsymbol{\alpha}_A^\wedge(t) & {}_F^A \mathbf{a}_A(t) \\ \mathbf{0}_{1 \times 3} & 0 \end{bmatrix} \quad (2.40)$$

where ${}_F^A \boldsymbol{\alpha}_A(t) \in T\mathfrak{so}(3)$ is an angular acceleration in the scaled-axis representation, and the linear acceleration is ${}_F^A \mathbf{a}_A(t) \in T^2\mathbb{R}^3 \equiv \mathbb{R}^3$.

From this point on, frames will dropped in the notation. For a body labelled x fixed to a frame $\{A\}$, ${}_F^A \mathbf{S}_A$, ${}_F^A \mathbf{T}_A$ and ${}_F^A \mathbf{W}_A$ will be denoted \mathbf{S}_x , \mathbf{T}_x and \mathbf{W}_x .

2.1.6 Rigid Body Kinematics

The dynamics of the screw, twist and wrench matrices as they are defined in section 2.1.5 are governed by the following ordinary differential equations (ODEs),

$$\frac{d}{dt} \mathbf{S}(t) = \mathbf{S}(t) \mathbf{T}(t) \quad (2.41)$$

$$\frac{d}{dt} \mathbf{T}(t) = \mathbf{W}(t) \quad (2.42)$$

$$\frac{d}{dt} \mathbf{W}(t) = \mathbf{f}(t) \quad (2.43)$$

where the function $\mathbf{f}(t)$ is known.

2.1.7 Scanning Laser Range-finder Dynamic Model

A scanning laser range-finder is a sensor that measures the distance to the nearest object in a certain direction. Consider such a sensor fixed to a moving rigid body. The pose of

the sensor s is defined by \mathbf{S}_s , \mathbf{T}_s and \mathbf{W}_s . The scanning direction of the sensor is a unit vector ${}^A\mathbf{d}(t) \in S^2$ defined in the body fixed frame $\{A\}$.

The sensor provides measurement of the range $r(t) \in \mathbb{R}^{0+}$ from ${}^F\mathbf{p}_A(t)$ to the nearest object in the environment in the direction ${}^F\mathbf{d}(t) = {}^F\mathbf{R}_A(t) {}^A\mathbf{d}(t)$.

The function ${}^A\mathbf{d}(t)$ determines the scanning behaviour of the sensor and depends on the specific model used. The scanning model for the Hokuyo UBG-04LX-FO1 used in this research is provided in section 4.1.2.2.

2.2 State Observers

2.2.1 Luenberger observers

An observer is a filter that is used to estimate the state of a dynamic system. The state x can be chosen as some set of variables governed by the system. In real-world conditions, the system is often infinite-dimensional.

The real system, known as the *plant* is represented with a *model*. In most cases, some simplification of the plant must be performed to produce the model.

An observer provides an estimate \hat{x} of the state $x \in \mathbb{R}^n$ of the model, given an output $y \in \mathbb{R}^m$ and a system input $u \in \mathbb{R}^p$. The dynamics of a nonlinear system are modelled with a nonlinear function f of dimension n .

$$\dot{x}(t) = f(x(t), u(t)) \quad (2.44)$$

The state output y can also be conceptualised as a measurement of the state x , where the measurement function g is of dimension m .

$$y(t) = g(x(t), u(t)) \quad (2.45)$$

An observer employs an innovation function $L : \mathbb{R}^m \rightarrow \mathbb{R}^n$ to update a state estimate \hat{x} using the difference between the measurement $y(t)$ and the predicted measurement \hat{y} .

$$\dot{\hat{x}} = f(\hat{x}, u(t)) + L(y(t) - \hat{y}(t)) \quad (2.46)$$

$$\hat{y}(t) = g(\hat{x}(t), u(t)) \quad (2.47)$$

This form of observer was developed by Luenberger [24], and is often referred to as a *Luenberger observer*. Combining the observer equation with the measurement prediction function g gives the state observer as

$$\dot{\hat{x}} = f(\hat{x}, u(t)) + L(y(t) - g(\hat{x}(t), u(t))) \quad (2.48)$$

The goal is to choose an innovation function L that reduces the observer error $e(t) = x(t) - \hat{x}(t)$ to 0.

2.2.2 Symmetry-preserving observers

If the function f governing the dynamics of the state is invariant to the action of a Lie group \mathbf{G} , invariant observer has the form

$$\dot{\hat{x}} = h(\hat{x}, u(t), y(t) - \hat{y}(t)) \quad (2.49)$$

where the function h is also invariant to actions of \mathbf{G} . For nonlinear systems, the result is often improved global convergence properties in comparison to a traditional Luenberger observer.

Chapter 3

Problem Statement

This project is part of a larger research direction at the ANU Research School of Engineering that will develop a theory of infinite-dimensional, symmetry preserving observers. As an initial exploration of this open problem, the central goals of this project are to:

- gain an understanding of how dense sensors can be used to take measurements of the state of infinite-dimensional systems;
- gain an insight into how symmetry-preserving observers can be used to better observe nonlinear infinite-dimensional systems
- uncover pertinent directions for future research in this area; where a theory of infinite-dimensional, symmetry preserving observers would be useful
- investigate if a sparse sensor can be used in a manner that approximates the capabilities of a dense sensor in the measurement of an infinite-dimensional state.

The approach taken to achieve these goals will be to design and implement an observer for a simplified system that still captures some components of the overall research goals. The state variable to be estimated will be finite-dimensional, and thus the observer will be finite-dimensional. However, the sensor will still provide information of an infinite dimensional system. In this way, the problem is similar to the dense optical flow estimation by Adarve et al. [23]. Initially, the observer innovation function will not be designed to be invariant. As a first step, this research will investigate correction schemes that converge locally. A future work package will be to adjust the update function to respect the symmetries of the system and achieve more global convergence properties.

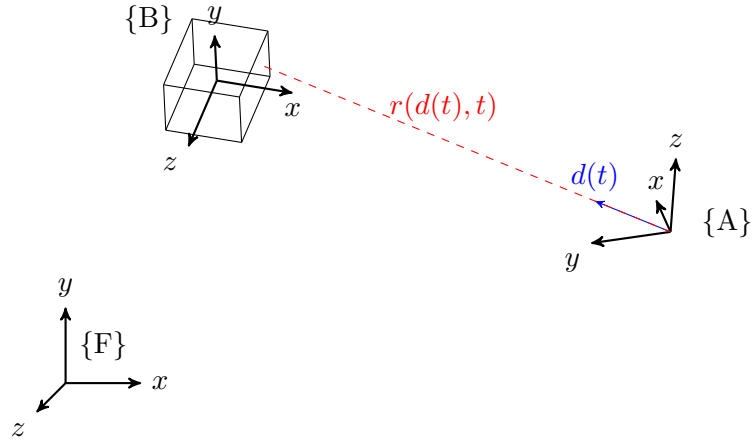


Figure 3.1: Range measurements of a cube from a depth sensor

3.1 Estimating the pose and size of a cube from sparse range measurements

A situation in which an infinite dimensional observer would be useful is in the estimation of the pose of an object of unknown size moving in an environment of unknown state. For example, consider an autonomous robot deployed in an agricultural survey, which must determine the position and size of a certain crop. Using a geometric model for the general shape of the crop, an aerial vehicle that could routinely detect and characterise the position and size of specimens would be useful in monitoring growth and during harvesting.

The problem to be investigated is shown in Figure 3.1. A 2D scanning range sensor moves through an environment consisting of a target object of known shape, in this case a rigid cube, and an unknown background which may be an infinite dimensional dynamic system. The state of the sensor is known, but the states of the cube and background environment are unknown. The goal is to use the state of the sensor and the range measurements it provides to estimate the state of the cube.

The frames used to describe the motion of the rigid bodies in this problem are:

- $\{F\}$ - the inertial (fixed) frame. For the purposes of this problem, the inertial frame is a frame whose motion is negligible. For the practical experiment this frame will be fixed to the ground.
- $\{A\}$ - the frame fixed to the sensor. The origin of this frame is the centre of rotation of the sensor's scan direction. The axes of $\{A\}$ are fixed to the sensor according to Figure 4.1 in chapter 4. The transformation from $\{F\}$ to $\{A\}$ at time t is defined by

the screw matrix of the sensor $\mathbf{S}_s(t)$.

- $\{B\}$ - the frame fixed to the cube. The origin of $\{B\}$ coincides with the centre of the cube and is aligned so that each axis intersects with the centre of a face of the cube. The transformation from $\{F\}$ to $\{B\}$ at time t is defined by the screw matrix of the cube $\mathbf{S}_c(t)$.

The sensor provides measurements of the range r to the nearest object from the sensor (either the cube or the background) in the direction $\mathbf{d}(t)$. These measurements can be considered sparse because the distance to just a single point is returned at each time step.

The state of the sensor $\mathbf{X}_s(t)$ is defined as:

$$\mathbf{X}_s(t) = \{{}^F_S \mathbf{S}_A(t), {}^F_T \mathbf{T}_A(t), {}^F_W \mathbf{W}_A(t), {}^A \mathbf{d}(t)\} \quad (3.1)$$

The screw matrix represents the transformation from $\{A\}$ to $\{F\}$, defined in $\{F\}$. The twist and wrench matrices, as well as the scan direction $\mathbf{d}(t)$ are defined in terms of $\{A\}$. For simplicity, this will be denoted

$$\mathbf{X}_s(t) = \{\mathbf{S}_s(t), \mathbf{T}_s(t), \mathbf{W}_s(t), {}^A \mathbf{d}(t)\} \quad (3.2)$$

The direction of measurement ${}^A \mathbf{d}(t)$ varies as a rotation about the z-axis of $\{A\}$. This 2D scanning motion depends on the model of the sensor used and is described in more detail in section 4.1.2.2. For simplification, the motion of the sensor itself with respect to $\{F\}$ will be limited to rotation about the y -axis of $\{F\}$.

The state of cube $\mathbf{X}_c(t)$ is defined as

$$\mathbf{X}_c(t) = \{{}^F_S \mathbf{S}_B(t), {}^F_T \mathbf{T}_B(t), {}^F_W \mathbf{W}_B(t), s\} \quad (3.3)$$

For simplicity, this will be denoted

$$\mathbf{X}_c(t) = \{\mathbf{S}_c(t), \mathbf{T}_c(t), \mathbf{W}_c(t), s\} \quad (3.4)$$

The range measurements do not indicate whether the object detected is the cube or the background. Though the state of the cube and environment remain unknown, for simplification, it is assumed that either:

- the cube is within a distance r_{max} from the sensor and the background is at least a distance r_{max} away
- these target object and background do not touch or overlap and their surfaces are continuous functions on \mathbb{R}^3

These assumptions will be used to separate range measurements corresponding to the cube from those corresponding to the background. Only range measurements corresponding to the cube will be used in the observer innovation step. For simulated data, only the first assumption is necessary. For experimental data sets the environment is more complex so the second assumption is required to identify range measurements corresponding to the cube.

The aim is to design a nonlinear observer function f which estimates the state of the cube from the pose of the sensor, scan direction s and range measurement \tilde{r} and measurement prediction \hat{r} .

$$\hat{\mathbf{X}}_c(k+1) = f(\mathbf{X}_s(t), \hat{\mathbf{X}}_c(k), \tilde{r}(t), \hat{r}(t)) \quad (3.5)$$

This observer formulation differs from that provided in equation 2.46 in that no state input is present in the system and more importantly, \tilde{r} and \hat{r} are provided as separate terms. Though a true Luenberger observer is driven by the output difference $\tilde{r} - \hat{r}$, such a scheme is not possible due to the way the problem has been simplified. Since range measurements corresponding to the background are discarded, the term $\tilde{r} - \hat{r}$ is undefined unless both ranges correspond to the cube. Such a limitation would make correcting differences in position and size particularly difficult.

A simulation toolbox will be implemented to simulate range measurements of rigid bodies using a scanning range sensor. The observer implementation will be implemented and its performance tested under a range of conditions.

Experimental validation will be performed by taking measurements of a known environment using the Hokuyo UBG-04LX-FO1 scanning laser range-finder. These measurements will be used to quantify the performance of the observer under real-world conditions.

The observer implementation will be considered successful if it is able to converges to the true cube state around a local neighbourhood. Since an invariant observer is not being implemented, global convergence is not expected.

3.2 Deliverables

The project deliverables are:

- implement a toolbox to simulate range measurements of rigid bodies;
- design an observer to estimate cube state from sparse range measurements;
- produce and test a software implementation of the observer;
- validate the observer performance by collecting experimental data;
- present the research in a report and presentation.

Chapter 4

Observer Simulation

4.1 Implementation

A simulation toolbox was implemented in Matlab to model scanning laser range-finder measurements and test observer schemes. The main components of the simulation are:

- rigid body trajectory computation;
- solid object modelling;
- range measurement simulation;
- noise modelling;
- observer implementation.

The notation employed here and throughout the rest of the report uses the following conventions:

- Single values are denoted by plain text;
- Vectors are denoted in bold lowercase;
- Matrices are denoted in bold uppercase;
- An array formed by replicating a variable \mathbf{a} in an $n \times m$ block array is denoted $\mathbf{a}_{n \times m}$.
- In many cases, a variable such as the sensor position $\mathbf{p}_s(t)$ represents a set of elements, each corresponding to the value at a certain time t . These will be referred to by the form of the value at a single time. For example, a matrix where each column represents a different position vector is used to represent $\mathbf{p}_s(t)$, but it will be described as a vector as this is the form of a single position.

Algorithm 1: Scanning range-finder and state observer simulation

Data:

n_{steps} - number of time steps in simulation
 \mathbf{X}_s - sensor pose and scan direction
 \mathbf{X}_e - cube and background pose, points and triangles
 $\hat{\mathbf{X}}_c$ - estimate of the pose and size of the cube
 c - (true/false) current range measurement is of cube or not
 \mathbf{r} - ground truth range
 $\tilde{\mathbf{r}}$ - measured range
 $\hat{\mathbf{r}}$ - range predicted from state estimate
 α - angle of incidence for each range measurement
 \mathbf{m} - index of triangle measured
 θ - scan angle in sensor frame
 Θ - set of scan angles that return range measurement

```

1 begin
2   settings ← loadsettings
3    $\mathbf{X}_s \leftarrow \text{initialisesensor}(settings)$ 
4    $\mathbf{X}_e \leftarrow \text{initialiseenvironment}(settings)$ 
5   initialiseobserver
6   for  $ii \leftarrow 1$  to  $n_{steps}$  do
7     if  $\theta[ii] \in \Theta$  then
8       |  $[\mathbf{r}[ii], \alpha[ii], \mathbf{m}[ii]] \leftarrow \text{computerange}(\mathbf{X}_s[ii], \mathbf{X}_e[ii])$ 
9     end
10   end
11    $\tilde{\mathbf{r}} = \text{addnoise}(\mathbf{r}, \alpha, \mathbf{m}, settings)$ 
12   for  $ii \leftarrow 1$  to  $n_{steps}$  do
13     |  $\hat{\mathbf{X}}_c[ii + 1] \leftarrow \text{estimatestate}(\hat{\mathbf{X}}_c[ii])$ 
14     | if  $\theta[ii] \in \Theta$  then
15       |   |  $\hat{\mathbf{r}}[ii] \leftarrow \text{computerange}(\mathbf{X}_s[ii], \hat{\mathbf{X}}_c[ii])$ 
16       |   |  $c \leftarrow \text{identifyobject}(c, \tilde{\mathbf{r}})$ 
17       |   | if  $c$  then
18         |   |   |  $\hat{\mathbf{X}}_c[ii + 1] \leftarrow \text{updatestate}(\hat{\mathbf{X}}_c[ii + 1], \mathbf{X}_s[ii], \hat{\mathbf{r}}, \tilde{\mathbf{r}})$ 
19       |   | end
20     | end
21   end
22 end

```

A high level description of the simulation is provided in Algorithm 1. First, a settings file is loaded. The most important settings determined here are the trajectories of the sensor and environment objects, the scanning behaviour of the sensor and the observer update function. Next, the sensor class instance is initialised with `initialisesensor`. This requires computation of the pose and scanning directions of the sensor over time. Similarly, initialisation of the environment through `initialiseenvironment` requires computation of the pose of each rigid body comprising it. The surfaces of the bodies are then represented with a set of points and corresponding triangles. The position of each point with respect to the inertial frame $\{F\}$ is computed at each time step. The settings file provides the initial conditions with which the observer is initialised in `initialiseobserver`. Beginning on line 6, the state of the sensor and environment are used to compute the ground truth range measurements \mathbf{r} at each time step. The incidence angle between the scan direction and object, as well as the index of the triangle hit are also stored as they will be required for sensor noise modelling. This is performed with a parallel `for` loop to speed up computation. Line 7 ensures ranges are only computed when the current scan direction is within the sensor's field of view. In line 11, noise is simulated and added to the ground truth ranges to produce the measured ranges $\tilde{\mathbf{r}}$. The `for` loop beginning on line 12 begins the observer simulation. At each time step, `estimatestate` estimates the state of the cube $\hat{\mathbf{X}}_c$ from the previous state with the kinematics model in 2.1.6. From the sensor state \mathbf{X}_s and the estimated state of the cube $\hat{\mathbf{X}}_c$, `computerange` is used to determine the predicted range measurement $\hat{\mathbf{r}}$. The variable c indicates whether the current range measurement corresponds to the cube or the background. On line 16 the measured ranges and previous value of c are used to determine whether the current measurement corresponds to the cube. If it does, the cube state estimate $\hat{\mathbf{X}}_c$ is updated using the previous state estimate, current sensor state, and the predicted and measured ranges.

4.1.1 Rigid Body Motion

To simulate range measurements the pose of the sensor and the objects comprising the environment must be computed at each time step. The computations required to do so can be reduced by taking into account the kinds of motion that must be simulated. This section details how the pose of the sensor and objects is represented and computed, which is used in the functions `initialisesensor`, `initialiseenvironment` and `estimatestate` referenced in Algorithm 1.

The observer actually computes the *relative* position between the sensor and cube and simply uses knowledge of the sensor pose to determine the pose of the cube in the inertial frame. There is no need to simulate complex sensor motions because the motion of the cube can be adjusted to achieve the same result. The only requirement of the sensor motion is that measurements of a large range of the environment are acquired to ensure that the entire target object can be viewed. The scanning behaviour of the sensor is to rotate about the z -axis of the body fixed frame $\{A\}$. To provide a rectangular field of view, the motion of the sensor is therefore limited to constant velocity rotation about y -axis of inertial frame $\{F\}$.

The environment is modelled with two rigid bodies: a cube to be observed as the target object, and a stationary rectangular prism enclosing the sensor and cube acting as the background. The various cube motions that will be simulated to test the observer's performance can be classed in terms of the wrench matrix of the cube as either

1. $\mathbf{W}_c = \mathbf{0}$
2. $\mathbf{W}_c \neq \mathbf{0}$

For case 1. the wrench and screw are constant so only the initial value is required. It is more efficient to represent the pose of a rigid body with just position and orientation in this case. The pose can be quickly computed by interpolating between an initial and final pose. For case 2. the screw, twist and wrench must be integrated numerically.

4.1.1.1 Interpolation

For the case of zero wrench, the pose of the body can be represented with a position vector \mathbf{p}_i and an orientation quaternion \mathbf{q}_i . A trajectory of k poses at times $\mathbf{t} = [t_1 \ t_2 \ t_3 \ \dots \ t_k]$, is computed by interpolating from an initial pose $\{\mathbf{p}_0, \mathbf{q}_0\}$ to a final pose $\{\mathbf{p}_k, \mathbf{q}_k\}$.

The array of position vectors $\mathbf{P} = [\mathbf{p}_1 \ \mathbf{p}_2 \ \mathbf{p}_3 \ \dots \ \mathbf{p}_k]$ are computed with:

$$\mathbf{P} = (\mathbf{1}_{3 \times k})\mathbf{p}_1 + (\mathbf{p}_k - \mathbf{p}_1) \frac{\mathbf{t} - t_1(\mathbf{1}_{1 \times k})}{t_k - t_1} \quad (4.1)$$

Spherical linear interpolation is used to compute the array of orientation quaternions

$\mathbf{Q} = [\mathbf{q}_1 \ \mathbf{q}_2 \ \mathbf{q}_3 \ \dots \ \mathbf{q}_k]$ at each time step:

$$\mathbf{Q} = \frac{\mathbf{q}_1 \sin((\mathbf{1}_{[1 \times k]} - \mathbf{t})\theta) + \mathbf{q}_k \sin(\mathbf{t}\theta)}{\sin(\theta)} \quad (4.2)$$

where

$$\theta = \cos^{-1}(\mathbf{q}_1 \cdot \mathbf{q}_k) \quad (4.3)$$

This interpolation method is used to compute the trajectory of the sensor. To acquire multiple views of the entire cube, the sensor must pan back and forth several times. This is achieved by first reversing the trajectory and concatenating with the original to produce the looped trajectories \mathbf{P}_{loop} and \mathbf{Q}_{loop} :

$$\mathbf{P}_{loop} = [\mathbf{p}_1 \ \mathbf{p}_2 \ \mathbf{p}_3 \ \dots \ \mathbf{p}_k \ \mathbf{p}_k \ \mathbf{p}_{k-1} \ \mathbf{p}_{k-2} \ \dots \ \mathbf{p}_1] \quad (4.4)$$

$$\mathbf{Q}_{loop} = [\mathbf{q}_1 \ \mathbf{q}_2 \ \mathbf{q}_3 \ \dots \ \mathbf{q}_k \ \mathbf{q}_k \ \mathbf{q}_{k-1} \ \mathbf{q}_{k-2} \ \dots \ \mathbf{q}_1] \quad (4.5)$$

This looped trajectory is repeated k times to produce multiple back and forth scans:

$$\mathbf{P} = (\mathbf{P}_{loop})_{1 \times k} \quad (4.6)$$

$$\mathbf{Q} = (\mathbf{Q}_{loop})_{1 \times k} \quad (4.7)$$

4.1.1.2 Numerical Integration

The time evolution of the screw, twist and wrench is computed iteratively from initial conditions by numerically integrating the ODEs in section 2.1.6. For a rigid body with an associated reference frame $\{X\}$, moving with constant acceleration:

$$\mathbf{S}_X(t + \delta t) = \mathbf{S}_X(t) \exp(\delta t \mathbf{T}_X(t)) \quad (4.8)$$

$$\mathbf{T}_X(t + \delta t) = \mathbf{T}_X(t) + \delta t \mathbf{W}_X(t) \quad (4.9)$$

$$\mathbf{W}_X(t + \delta t) = \mathbf{W}_X(t) \quad (4.10)$$

Though a higher order integration method, such as Runge-Kutta could be used to compute a trajectory that more accurately represents a constant acceleration, this is not strictly necessary. The observer performance is unlikely to be affected by how constant the acceleration is. Furthermore, it is likely that the experimentally collected data will have even larger variations in acceleration.

To simplify the code, the position vector and orientation quaternion are computed from the screw matrix. This allows the same functions to be used in either the interpolation or numerical integration cases. Rotating the points that make up the rigid objects can also be done more compactly with quaternions.

4.1.2 Sensor modelling: `initialisesensor`

The motion model below is used to compute the pose of the sensor. The scanning model is used to compute the set of scanning directions. These actions are performed in the `initialisesensor` function in Algorithm 1

4.1.2.1 Motion

The state of the sensor $\mathbf{X}_s(t)$ consists of terms corresponding to its motion and scanning operation. Since the motion of the sensor is restricted to zero acceleration, the state of sensor can be computed with the interpolation method and represented with position, orientation and scanning direction.

$$\mathbf{X}_s(t) = \{\mathbf{p}_s(t), \mathbf{q}_s(t), {}^A\mathbf{d}(t)\} \quad (4.11)$$

Since it has a stationary position, the position of the sensor over time is fixed at the origin of the inertial frame $\{F\}$.

$$\mathbf{p}_1 = \mathbf{p}_2 = \mathbf{p}_3 = \dots = \mathbf{p}_k = \begin{bmatrix} 0 \\ 0 \\ 0 \end{bmatrix} \quad (4.12)$$

The sensor rotates between $-\phi$ and ϕ about the y -axis of inertial frame $\{F\}$. Thus, its orientation is computed by interpolating between \mathbf{q}_1 and \mathbf{q}_k with equation 4.2.

$$\mathbf{q}_1 = \begin{bmatrix} \cos(-\phi/2) \\ 0 \\ \sin(-\phi/2) \\ 1 \\ 0 \end{bmatrix} = \begin{bmatrix} \cos(\phi/2) \\ 0 \\ -\sin(\phi/2) \\ 0 \end{bmatrix} \quad (4.13)$$

$$\mathbf{q}_k = \begin{bmatrix} \cos(\phi/2) \\ 0 \\ \sin(\phi/2) \\ 1 \\ 0 \end{bmatrix} = \begin{bmatrix} \cos(\phi/2) \\ 0 \\ \sin(\phi/2) \\ 0 \end{bmatrix} \quad (4.14)$$

4.1.2.2 Scanning

The scanning behaviour of the sensor depends on the particular model used. The *Hokuyo UBG-04LX-F01* scanning laser range-finder will be modelled as it was the sensor used to conduct experiments in this project. This sensor produces a 785nm laser beam, projected at a precise direction. It measures the characteristics of the reflected beam to determine the position to the nearest object in the direction of the beam. The direction of the laser beam is varied by reflecting it off a rotating mirror. The rotation means that the beam direction effectively rotates with a constant velocity in a single plane. A portion of the field of view of the laser beam is obscured, so measurements will not be returned in a certain region of each revolution.

The vector ${}^A\mathbf{d}(t)$ will be used to model this scanning behaviour. To accurately model this, the following parameters are used:

- field of view Θ : The vector ${}^A\mathbf{d}(t)$ rotates anti-clockwise about the z axis of the sensor frame $\{A\}$. Measurements are only taken when the scan angle about is between $-\theta$ and θ about the $-z$ -axis of the sensor frame $\{A\}$. In practice, the field of view is implemented as the start angle $-\theta$, direction of rotation and angular range 2θ .
- number of scans n_{scans} : This represents the number of scan angles in a single revolution. Since measurements are limited by the field of view of the sensor, the actual number of measurements per second is $n_{ranges} = \frac{2\theta}{2\pi} n_{scans}$. The angular resolution is $d\theta = \frac{2\pi}{n_{scans}}$.

- revolutions per second Ω : This is measured in Hz and gives the length of each time step $d\tau = \frac{1}{n_{scans}\Omega}$
- n_{loops} : The number of back and forth repeats of the sensor trajectory.

From these parameters the scanning direction ${}^A\mathbf{d}(t)$ is created. At each time t , ${}^A\mathbf{d}(t)$ is either a unit vector indicating the direction of measurement in the sensor frame, or has $\mathbf{0}$ magnitude, corresponding to when ${}^A\mathbf{d}(t)$ is outside the field of view and the sensor is not returning a measurement.

$${}^A\mathbf{d}(t) = \begin{cases} \begin{bmatrix} \cos(-\theta + 2\pi t') \\ -\sin(-\theta + 2\pi t') \\ 0 \end{bmatrix} & \text{if } t' \leq \theta/\pi, t' = k\delta\tau \forall k \in \mathbb{N} \\ \mathbf{0}_{3 \times 1} & \text{if } t' > \theta/\pi, t' \neq k\delta\tau \forall k \in \mathbb{N} \end{cases} \quad (4.15)$$

where

$$t' = \mod(t, 1/d\theta) d\theta \quad (4.16)$$

Figure 4.1 shows the frame $\{A\}$ fixed to the sensor and the scan direction ${}^A\mathbf{d}(t)$. At time $t' = 0$, the first scan direction ${}^A\mathbf{d}_0$ has an angular displacement of $-\theta$ about the z -axis from the forward facing x -direction. After each time step $d\tau$, the scan direction rotates by $d\theta$ about the z -axis. There are n_{ranges} scan directions within the field of view of the sensor. The entire revolution is divided into n_{scans} scan directions.

To simulate range measurements, the scan direction is required in the inertial frame $\{F\}$. This is computed by multiplying with the screw matrix of the sensor.

$$\begin{aligned} {}^F\mathbf{d}'(t) &= \mathbf{S}_s(t) {}^A\mathbf{d}'(t) \\ &= {}^F\mathbf{S}_A(t) {}^A\mathbf{d}'(t) \end{aligned} \quad (4.17)$$

4.1.2.3 Hokuyo UBG-04LX-F01 Model

EDIT THIS PART

motion

-stationary, rotate between $-\pi/8$ to $\pi/8$ about y -axis. rotates at $\pi/4$ rad/s **sensor parameters** **fov** = π rad, from $\pi/2$ to $-\pi/2$ ie clockwise rotation ie rotates about $-z$ axis.

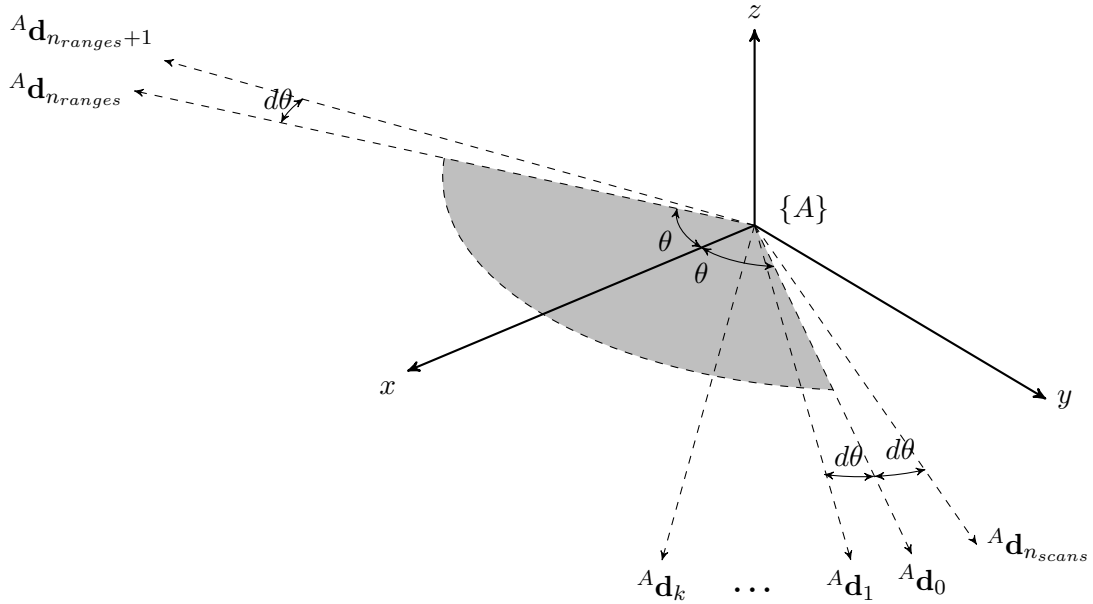


Figure 4.1: Scanning behaviour of the UBG-04LX-F01 and parameters used to model it

24 scans per sec, 512 measurements in scan, can think of this as having 1024 positions around revolution.

4.1.3 Environment Modelling: `initialiseenvironment`

The environment described in the problem formulation stated in Chapter 3 was an infinite dimensional system. Since the state variable to be estimated consists of just the cube pose and size and range measurements corresponding to the background are filtered out, the state of the background has no effect on the performance of the observer. To reduce computational load, the background will thus be modelled as a single object; a rigid rectangular prism enclosing both the sensor and cube. The entire state - cube and background - is now modelled as a finite dimensional state. However, the sensor is still taking measurements of a dense depth field on S^2 .

4.1.3.1 Motion

The pose of each object represents the pose of its centre of mass. As described in section 4.1.1 the pose is computed with interpolation for the case of zero wrench, and numerical integration in the case of non-zero wrench. The pose of the objects making up the environment is computed with the function `initialiseenvironment` in Algorithm 1. This

function also creates the points and triangles that model the surface of the objects which is described below.

4.1.3.2 Rigid Objects

The environment is represented with two rectangular prisms; the cube and a larger rectangular prism enclosing both the sensor and cube, to represent the background. These objects are modelled as an ordered set of 8 points in the inertial reference frame and an ordered set of 12 triangles formed by these points. Each triangle is represented by a set of 3 integers, indicating the index of the three points that make up its vertices.

The cube points in body frame $\{B\}$ are represented with the matrix ${}^B\mathbf{P}$.

$${}^B\mathbf{P} = \frac{1}{2}s \begin{bmatrix} -1 & -1 & -1 & -1 & 1 & 1 & 1 & 1 \\ -1 & -1 & 1 & 1 & -1 & -1 & 1 & 1 \\ -1 & 1 & -1 & 1 & -1 & 1 & -1 & 1 \end{bmatrix} \quad (4.18)$$

To represent these points in the inertial frame $\{F\}$, ${}^F\mathbf{P}$ is computed by rotating each point with the orientation quaternion of frame $\{B\}$ using equation 2.24 before adding the vector representing the translation of $\{B\}$ from $\{F\}$.

The triangles are represented with the matrix \mathbf{T} . Each triangle is represented by a row. The elements of these rows are the indexes of the points in ${}^F\mathbf{P}$ that form the three vertices of the triangle.

$$\mathbf{T} = \begin{bmatrix} 1 & 2 & 3 \\ 2 & 4 & 3 \\ 4 & 3 & 7 \\ 4 & 8 & 7 \\ 5 & 6 & 7 \\ 8 & 6 & 7 \\ 2 & 6 & 5 \\ 2 & 1 & 5 \\ 2 & 6 & 8 \\ 2 & 4 & 8 \\ 1 & 5 & 7 \\ 1 & 3 & 7 \end{bmatrix} \quad (4.19)$$

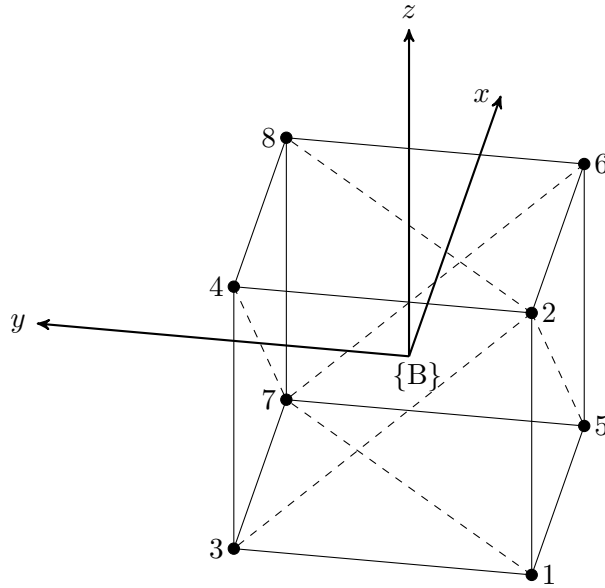


Figure 4.2: Cube modelled with an ordered set of points and corresponding triangles

The points and triangles are shown in Figure 4.2.

4.1.4 Measurement Modelling

4.1.4.1 Range Computation: `computerange`

This section describes the implementation used in the `computerange` function in Algorithm 1.

Given its screw matrix and scan direction (in the body fixed frame), the position of the sensor and its scan direction in the inertial frame are determined. The distance to the nearest environment object from the sensor along the scan direction is determined with the Möller-Trumbore ray-triangle intersection algorithm, shown in Algorithm 2.

Figure 4.3 shows a simplified scenario involving the intersection of a ray with a single triangle. In practice, the algorithm is vectorised to compute the intersections with a *set* of triangles. In this vectorised implementation, many variables represent a matrix whose columns are each vectors. These variables will still be described as vectors to emphasise the operation of the Möller-Trumbore algorithm, rather than the specific implementation details.

The output variables are first initialised to the case that there is no intersection with the

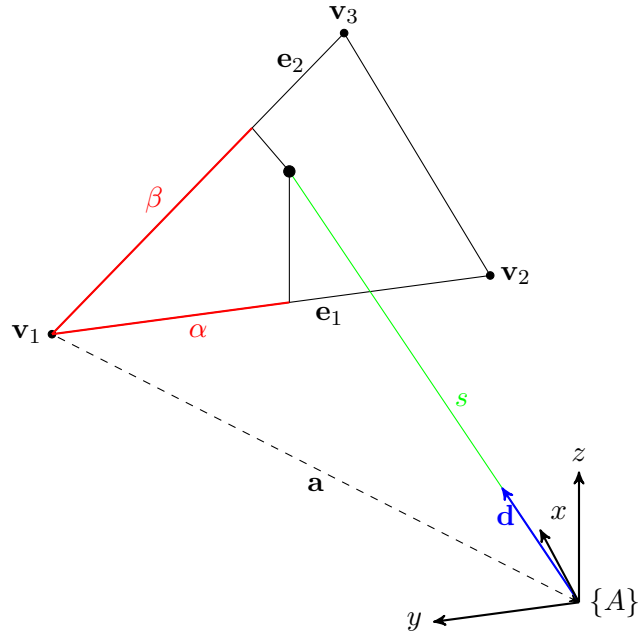


Figure 4.3: Ray-triangle intersection

scanning direction. x is set to `false` and the range, angle and triangle index outputs are set to return NaN.

On line 8, the set of points \mathbf{P} are indexed using the columns of the triangle matrix \mathbf{T} to extract the three vertices corresponding to each triangle. The vectors representing the edges sharing vertex \mathbf{V}_1 are computed. from triangles and points, extract vertices of each triangle. The vector \mathbf{A} computed on line 14 represents the translation from the ray origin \mathbf{o} to \mathbf{V}_1 .

The collection of vectors \mathbf{B} is computed on line 16 by taking the cross product of the scan direction \mathbf{d} and each edge \mathbf{E}_2 . The determinant δ of the matrix

$$\mathbf{M} = \begin{bmatrix} \mathbf{e}_1 \\ \mathbf{d} \\ \mathbf{e}_2 \end{bmatrix} \quad (4.20)$$

is computed on line 16. This is first used to determine if the scan direction \mathbf{d} lies in the plane of the triangle by checking if the determinant is close to zero. If so, no intersection can occur. The zero determinant values are then set to NaN to avoid a division by zero later.

Beginning on line 21, determinant δ is used to compute the barycentric coordinates α

and β , and the distance \mathbf{s} from the origin to the triangle plane along the scan direction \mathbf{d} .

The barycentric coordinates are used to determine if the intersection between the scan direction \mathbf{d} and the plane of the triangle lies within the triangle itself.

The vector \mathbf{x} on line 27 now indicates which triangles intersected with the scan direction. \mathbf{x} is used to mask the ranges to the triangles \mathbf{s} , to give \mathbf{r} ; the range to each intersecting triangle.

The minimum range r and triangle index m are determined before computing the angle of incidence θ between \mathbf{d} and the closest triangle.

4.1.4.2 Sensor Noise: `addnoise`

In Algorithm 1, the function `addnoise` takes the ground truth range measurements $r(t)$ and produces the noisy range measurements $\hat{r}(t)$ that the observer will actually receive. The noise function f_s is

$$\hat{r}(t) = f_s(r(t), \theta(t), \phi(k)) \quad (4.21)$$

where $\theta(t)$ is the incidence angle of the measurement at time t , ϕ represents the surface properties of the object k that was measured.

For the Hokuyo UBG-04LX-F01 sensor used, range measurements taken at various distances and incidence angles were used to estimate the noise model f_{UBG} which is provided in Section 5.1.

4.1.5 Observer Implementation

4.1.5.1 Estimate: `estimatestate`

The state of the cube at each time step is estimated using the numerical integration method described in section 4.1.1.2. This state estimation is implemented in the function `estimatestate` in Algorithm 1.

Algorithm 2: Möller-Trumbore ray-triangle intersection

```

input :  $\mathbf{o}$  - ray origin
       $\mathbf{d}$  - ray direction vector
       $\mathbf{P}$  - cube in inertial frame
       $\mathbf{T}$  - triangle matrix
output:  $x$  - True/False - measurement corresponds to object
       $r$  - distance to object in m
       $\theta$  - incidence angle in rad
       $m$  - index of triangle hit

1 begin
2   /* initialise outputs */ *
3    $x \leftarrow 0$ 
4    $r \leftarrow NaN$ 
5    $\theta \leftarrow NaN$ 
6    $m \leftarrow NaN$ 
7   /* triangle vertexes and edges */ *
8    $\mathbf{V}_1 \leftarrow \mathbf{P}[\mathbf{T}[:, 1]]$ 
9    $\mathbf{V}_2 \leftarrow \mathbf{P}[\mathbf{T}[:, 2]]$ 
10   $\mathbf{V}_3 \leftarrow \mathbf{P}[\mathbf{T}[:, 3]]$ 
11   $\mathbf{E}_1 \leftarrow \mathbf{V}_2 - \mathbf{V}_1$ 
12   $\mathbf{E}_2 \leftarrow \mathbf{V}_3 - \mathbf{V}_1$ 
13   $m = \text{size}(\mathbf{V}_1, 1)$ 
14   $\mathbf{A} \leftarrow \mathbf{o}_{[m \times 1]} - \mathbf{V}_1$ 
15  /* determinant */ *
16   $\mathbf{B} \leftarrow \mathbf{d}_{[m \times 1]} \times \mathbf{E}_2$ 
17   $\delta \leftarrow \mathbf{E}_1 \cdot \mathbf{B}$ 
18   $y \leftarrow |\delta| \leq 0$ 
19   $\delta[y] \leftarrow NaN$ 
20  /* barycentric coordinates */ *
21   $\alpha \leftarrow (\mathbf{A} \cdot \mathbf{B}) / \delta$ 
22   $\mathbf{Q} \leftarrow \mathbf{A} \times \mathbf{E}_1$  *(along dim 2)
23   $\beta \leftarrow (\mathbf{d}_{[n \times 1]} \cdot \mathbf{Q}) / \delta$  *(along dim 2)
24   $s \leftarrow (\mathbf{E}_2 \cdot \mathbf{Q}) / \delta$ 
25  /* intersection vector */ *
26   $\mathbf{z} \leftarrow \mathbf{y}$  and  $(\alpha \geq 0)$  and  $(\beta \geq 0)$  and  $(\alpha + \beta \leq 1)$ 
27   $\mathbf{x} \leftarrow \mathbf{z}$  and  $(s \geq 0)$ 
28  if any( $\mathbf{x}$ ) then
29     $x \leftarrow 1$ 
30     $\mathbf{x}[\mathbf{not} \mathbf{x}] \leftarrow NaN$ 
31     $\mathbf{r} = \mathbf{s} \circ \mathbf{x}$ 
32     $r = \min(\mathbf{r})$ 
33     $m = \text{find}(\mathbf{r} = r, 1)$ 
34     $\mathbf{e}_1 \leftarrow \mathbf{E}_1[t, :]$ 
35     $\mathbf{e}_2 \leftarrow \mathbf{E}_2[t, :]$ 
36     $\mathbf{n} = \mathbf{e}_1 \times \mathbf{e}_2$ 
37     $\theta = \text{atan2}(|\mathbf{d} \times \mathbf{n}|, \mathbf{d} \cdot \mathbf{n})$ 
38     $\theta = \min(\theta, \pi - \theta)$ 
39  end
40 end

```

4.1.5.2 Object/background separation: `identifyobject`

The observer update function will use range measurements to estimate the state of the cube \mathbf{X}_c . In order to perform accurately, the observer must only use range measurements that correspond to the cube. The function `identifyobject` in Algorithm 1 uses range measurements and knowledge of the configuration of the environment to separate measurements of the cube and background.

The binary variable c indicates whether the current range measurement corresponds to cube ($c = \text{true}$) or the background ($c = \text{false}$). It is assumed that initially the sensor will be observing the background, so $c_0 = \text{false}$.

The scheme used to identify range measurements corresponding to the cube is shown in Algorithm 3. There are two assumptions that may be used.

1. The *difference assumption* relies on the assumption that the cube and background objects are continuous. Differences in consecutive range measurements larger than Δ_{max} indicate a discontinuity, implying that a new object is being measured. When this occurs, the value of c changes.
2. The *range assumption* is used when the maximum distance to the cube and minimum distance to the background are restricted. Range measurements within r_{max} correspond to the cube while larger ranges correspond to the background.

4.1.5.3 Update: `updatestate`

If the `identifyobject` function identifies a range measurement as corresponding to the cube, the `updatestate` function is used to update the state estimate of the cube $\hat{\mathbf{X}}_c$. $\hat{\mathbf{X}}_c$ is updated using the previous cube state estimate, current sensor state, and sets of measured and predicted range measurements chosen according to a set of indexes $\mathbf{a}(t)$.

$$\hat{\mathbf{X}}_c(k+1) = f(\mathbf{X}_s(t), \hat{\mathbf{X}}_c(k), \mathbf{r}(\mathbf{a}(t)), \hat{\mathbf{r}}(\mathbf{a}(t))) \quad (4.22)$$

The pose of $\hat{\mathbf{X}}_c$ is corrected by adjusting $\hat{\mathbf{S}}_c$, $\hat{\mathbf{T}}_c$ or $\hat{\mathbf{W}}_c$. The orientation is adjusted by rotating about an axis \mathbf{r}_{update} . The position is adjusted by translating in the direction of \mathbf{p}_{update} . \mathbf{r}_{update} and \mathbf{p}_{update} are scaled differently, depending on whether they are applied to $\hat{\mathbf{S}}_c$, $\hat{\mathbf{T}}_c$ or $\hat{\mathbf{W}}_c$. The size update s_{update} is independent of the pose update scheme

Algorithm 3: Target/background object separation

```

input : differenceAssumption - true/false
        rangeAssumption - true/false
         $\Delta_{max}$  - max diff between measurements of same object
         $r_{max}$  - max range for cube
         $c$  - true/false - current measurement is of cube
         $\mathbf{r}_{i+1}$  - distance to object at  $t = i + 1$ 
         $\mathbf{r}_i$  - distance to object at  $t = i$ 

output:  $c$  - true/false

1 begin
2   if differenceAssumption then
3     if  $|\mathbf{r}_{i+1} - \mathbf{r}_i| > \Delta_{max}$  then
4        $c = \text{mod}(c + 1, 2)$ 
5     end
6   end
7   if rangeAssumption then
8     if  $\mathbf{r}_{i+1} > r_{max}$  then
9        $c = 0$ 
10    end
11  end
12 end

```

used.

Input ranges:

A set of four range measurements forming a quadrilateral are used in the state update. The four ranges are chosen with an ordered sequence of indexes $\mathbf{u}(t)$. At a time step ii , the set of time steps used is in the update function is

$$\mathbf{u}(ii) = \{ii, (ii - 1), (ii - n_{scans}), (ii - 1 - n_{scans})\} \quad (4.23)$$

It is possible that the measured or predicted ranges do not exist for some time steps in $\mathbf{u}(ii)$, as the range may have corresponded to the background rather than the cube. Thus, the measurement indexes $\tilde{\mathbf{u}}(ii)$ and estimation indexes $\hat{\mathbf{u}}(ii)$ will be subsets of, but not necessarily congruent to $\mathbf{u}(ii)$.

Orientation update:

The method used to correct the orientation of the cube state estimate $\hat{\mathbf{X}}_c$ is shown in Figure 4.4.

In order to estimate the orientation of the cube, at least 3 ranges are required from both the prediction and measurement: $|\hat{\mathbf{u}}| \geq 3$ and $|\tilde{\mathbf{u}}| \geq 3$. If all four indexes are present, the

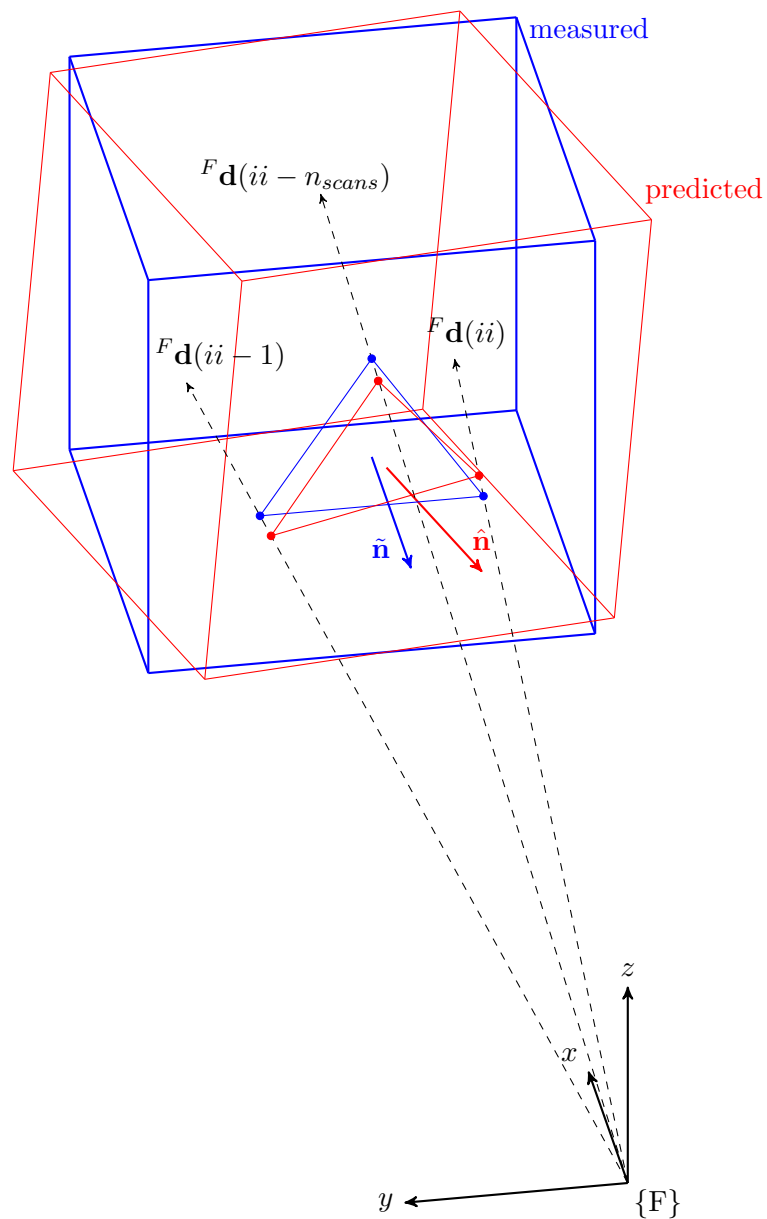


Figure 4.4: Orientation update scheme: intersection of the scan directions with the surfaces of the measured and predicted cubes are used to determine the surface normals.

ranges from the last time step ($ii - 1 - n_{scans}$) is ignored.

For both the measurement and prediction, the points of intersection ${}^F\mathbf{P}(\mathbf{u})$ between the set of scanning directions ${}^F\mathbf{D}(\mathbf{u})$ and the cube are computed using the set of range measurements $\mathbf{r}(\mathbf{u})$.

$${}^F\mathbf{P}(\mathbf{u}) = {}^F\mathbf{D}(\mathbf{u})\mathbf{r}(\mathbf{u}) \quad (4.24)$$

The normal to the plane formed by the three points is then computed.

$$\mathbf{n} = [{}^F\mathbf{P}(u_2) - {}^F\mathbf{P}(u_1)] \times [{}^F\mathbf{P}(u_3) - {}^F\mathbf{P}(u_1)] \quad (4.25)$$

Because a cube has 24 regular isometries, it is not necessary to effectively align the reference frames of the estimated and true cubes. Any face of the estimated cube can be aligned with any face of the true cube, and the maximum rotation correction will be $\pi/4$ radians.

The angle between the two normals ψ is computed as

$$\psi = \text{atan2}(|\hat{\mathbf{n}} \times \tilde{\mathbf{n}}|, \hat{\mathbf{n}} \cdot \tilde{\mathbf{n}}) \quad (4.26)$$

The axis \mathbf{r}_{update} that the estimated cube orientation $\hat{\mathbf{R}}_c$ will be rotated by is computed by taking the cross product of the predicted and measured normals. The direction of rotation is changed if the angle ψ between the two normals is greater than $\pi/4$ radians.

$$\mathbf{r}_{update} = \text{sign}\left(\frac{\pi}{4} - \psi\right) (\hat{\mathbf{n}} \times \tilde{\mathbf{n}}) \quad (4.27)$$

where

$$\text{sign}(x) = \begin{cases} 1 & \text{if } x \geq 0 \\ -1 & \text{if } x < 0 \end{cases} \quad (4.28)$$

To update the screw matrix $\hat{\mathbf{S}}_c$, \mathbf{r}_{update} is converted to a rotation matrix \mathbf{R}_{update} with Rodrigues' rotation formula (equation 2.19). The correction is then applied as:

$$\hat{\mathbf{R}}_c(k+1) = R_{scale}\mathbf{R}_{update}\hat{\mathbf{R}}_c(k) \quad (4.29)$$

To update via the screw or wrench, $\mathbf{r}_{update}^\wedge$ is scaled and then added to the angular velocity

or angular acceleration respectively.

$$\hat{\omega}_c^\wedge(k+1) = \hat{\omega}_c^\wedge(k) + \omega_{scale} \mathbf{r}_{update}^\wedge \quad (4.30)$$

$$\hat{\alpha}_c^\wedge(k+1) = \hat{\alpha}_c^\wedge(k) + \alpha_{scale} \mathbf{r}_{update}^\wedge \quad (4.31)$$

The chosen scale factor depends on whether \mathbf{r}_{update} is applied via $\hat{\mathbf{S}}_c$, $\hat{\mathbf{T}}_c$ or $\hat{\mathbf{W}}_c$.

Position update:

The method used to correct the position of $\hat{\mathbf{X}}_c$ is shown in Figure 4.5.

In order to estimate the position of the cube, at least 1 range measurement is required from both the prediction and measurement: $|\hat{\mathbf{u}}| \geq 1$ $|\tilde{\mathbf{u}}| \geq 1$. Additionally, scan directions at time steps ii , $(ii - 1)$ and $(ii - 1 - n_{scans})$ are required. The scan direction ${}^F\mathbf{d}(t)$ must be within the sensor's field of view at these time steps.

The points of intersection are calculated using equation 4.24. In Figure 4.5 all four scan directions intersect with the predicted cube state, but only one intersects with the measured cube. The average of these points is computed to give the mean estimated position $\hat{\mu}_{\mathbf{p}}$ and the mean measured position $\tilde{\mu}_{\mathbf{p}}$.

The x , y and z components of the update vector may very significantly in size due to the scanning behaviour of the sensor. It is necessary to scale the position update vector according to these components. The mean of all predicted and measured ranges μ_r is computed. Four points \mathbf{p}_0 , \mathbf{p}_1 , \mathbf{p}_2 and \mathbf{p}_3 are computed to be used in scaling:

$$\begin{aligned} \mathbf{p}_0 &= \mathbf{p}_s(t) = {}^F_F\mathbf{p}_A(t) \\ \mathbf{p}_1 &= \mu_r {}^F\mathbf{d}(ii) \\ \mathbf{p}_2 &= \mu_r {}^F\mathbf{d}(ii - 1) \\ \mathbf{p}_3 &= \mu_r {}^F\mathbf{d}(ii - 1 - n_{scans}) \end{aligned} \quad (4.32)$$

The update vector is computed by scaling the mean intersection points with these four points:

$$\mathbf{p}_{update} = \begin{bmatrix} \frac{1}{|\mathbf{p}_1 - \mathbf{p}_0|} & 0 & 0 \\ 0 & \frac{1}{|\mathbf{p}_2 - \mathbf{p}_1|} & 0 \\ 0 & 0 & \frac{1}{|\mathbf{p}_3 - \mathbf{p}_2|} \end{bmatrix} (\tilde{\mu}_{\mathbf{p}} - \hat{\mu}_{\mathbf{p}}) \quad (4.33)$$

The screw, twist and wrench are corrected using \mathbf{p}_{update} . The scaling factor used depends

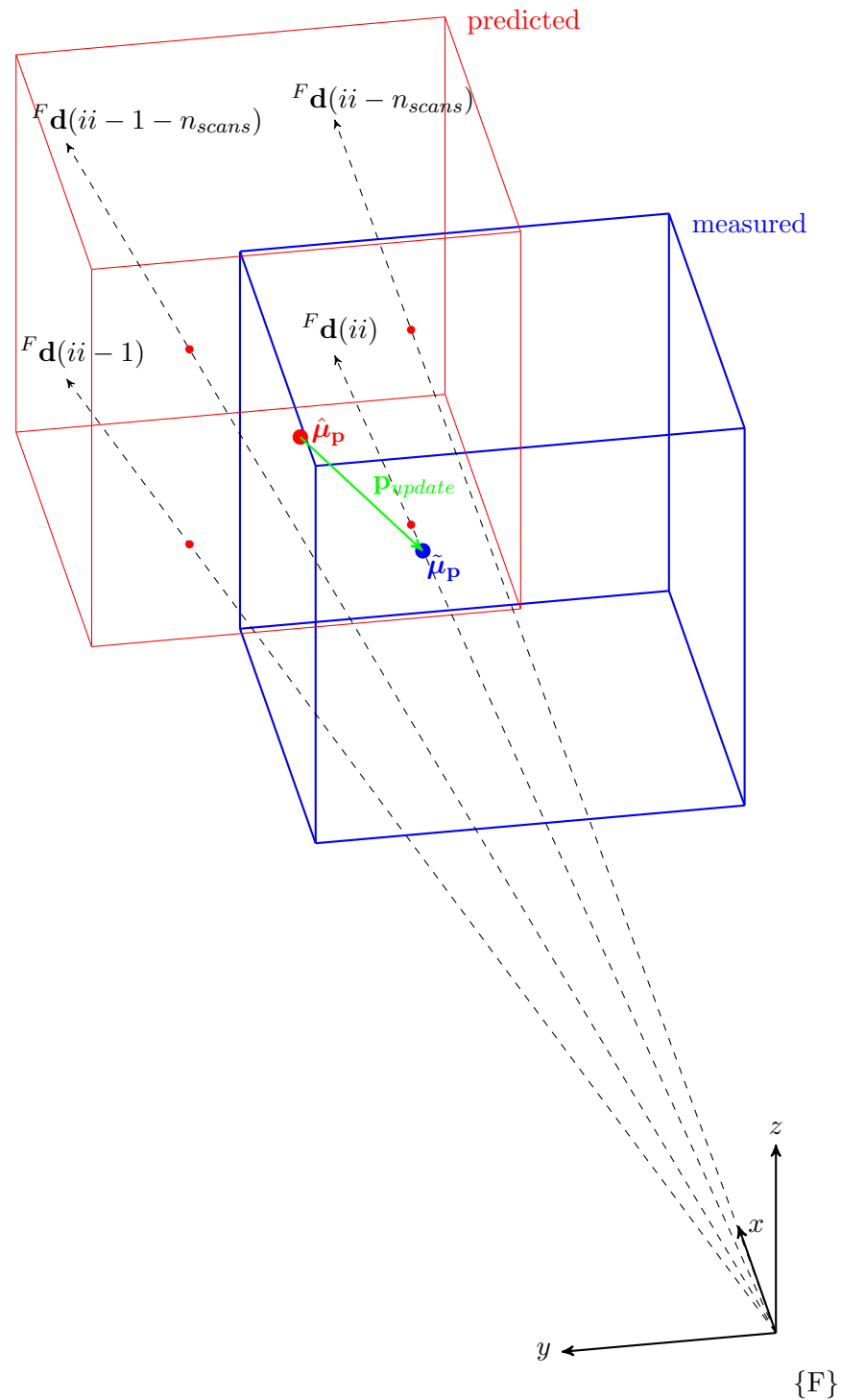


Figure 4.5: Position update

on whether the update is performed via the screw, twist or wrench.

$$\hat{\mathbf{p}}_c(k+1) = \hat{\mathbf{p}}_c(k) + p_{scale} \mathbf{p}_{update} \quad (4.34)$$

$$\hat{\mathbf{v}}_c(k+1) = \hat{\mathbf{v}}_c(k) + v_{scale} \mathbf{p}_{update} \quad (4.35)$$

$$\hat{\mathbf{a}}_c(k+1) = \hat{\mathbf{a}}_c(k) + a_{scale} \mathbf{p}_{update} \quad (4.36)$$

Size update:

In order to correct the size of the cube, at least 1 range measurement is required from both the prediction and measurement: $|\hat{\mathbf{u}}| \geq 1$ $|\tilde{\mathbf{u}}| \geq 1$. The size update scheme also differs based on the sets predicted and measured ranges.

For the case where a different pattern of ranges is observed ($\hat{\mathbf{u}} \neq \tilde{\mathbf{u}}$), the update method is shown in Figure 4.6.

The dot product from the vector \mathbf{p}_{update} computed for the position update and the current scan direction is taken:

$$s_{update} = \mathbf{p}_{update} \cdot {}^F\mathbf{d}(ii) \quad (4.37)$$

For the case where the same pattern of ranges is observer ($\hat{\mathbf{a}} = \tilde{\mathbf{a}}$), the update method is shown in Figure 4.7.

The size update is taken as the difference in the means of the measured and predicted ranges:

$$s_{update} = \tilde{\mu}_r - \hat{\mu}_r \quad (4.38)$$

In both cases, the cube size estimate is updated by scaling s_{update} and adding this to the previous estimate:

$$s(k+1) = s(k) + s_{scale} s_{update} \quad (4.39)$$

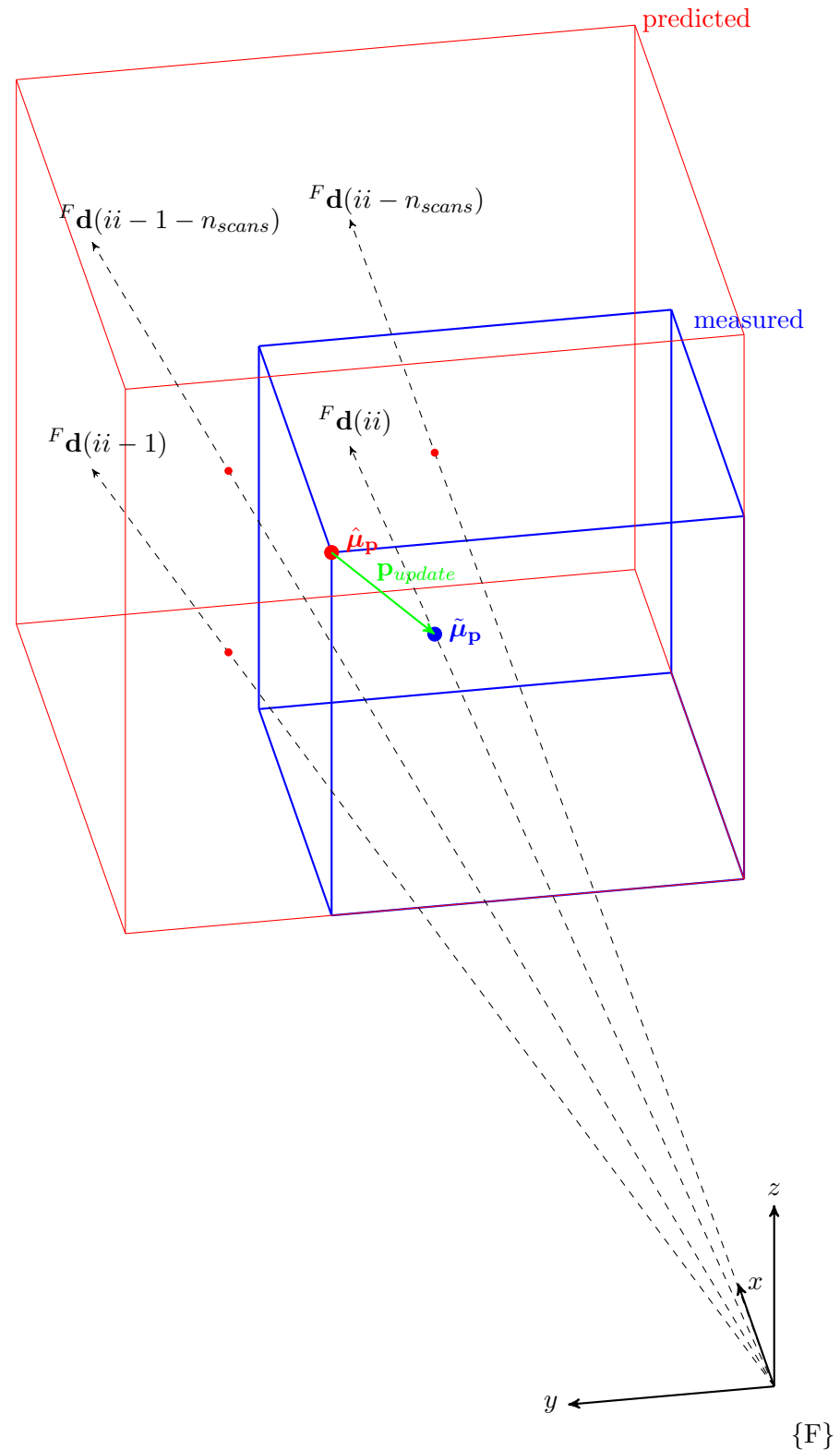


Figure 4.6: Size update - case 1

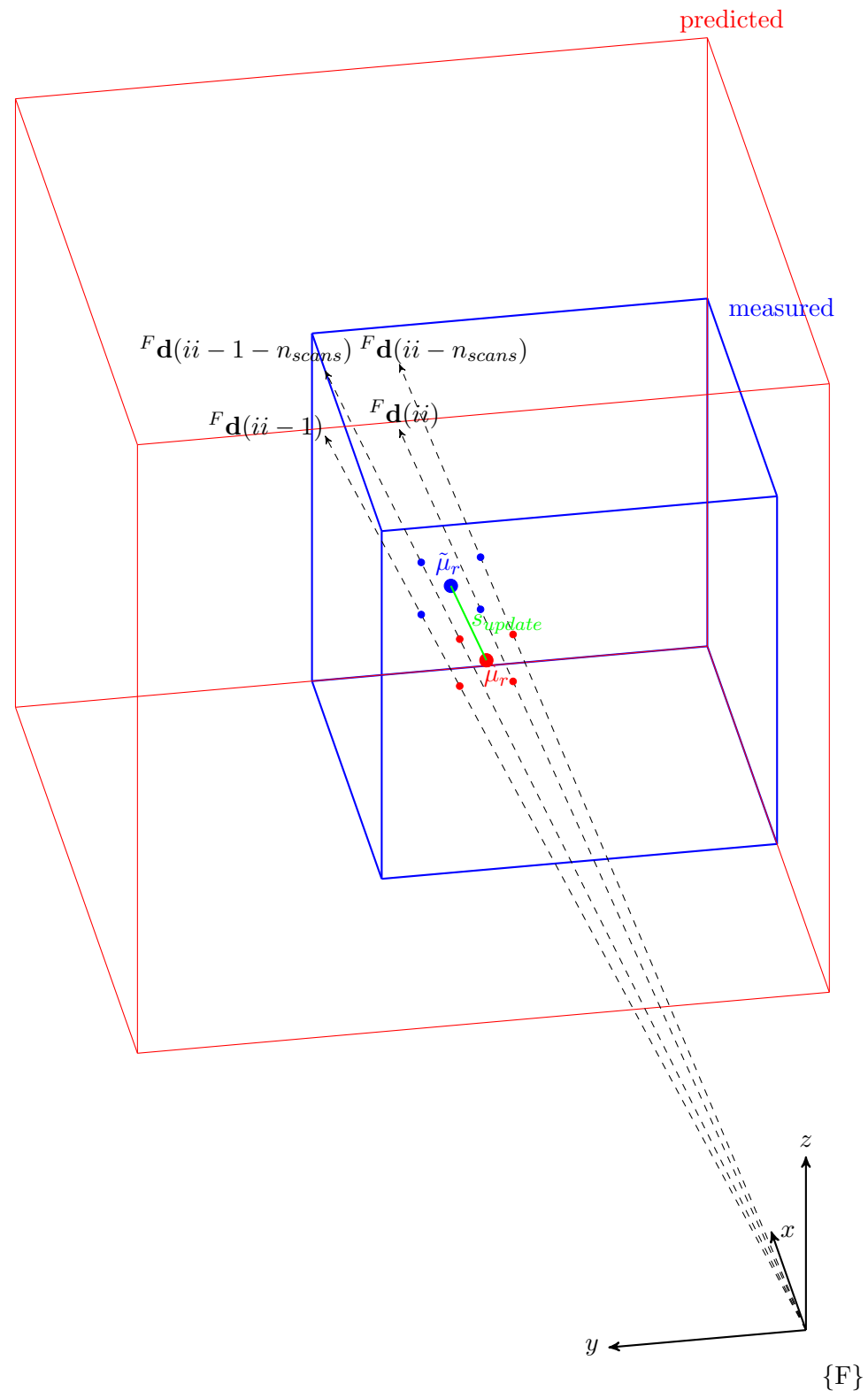


Figure 4.7: Size update - case 2

4.2 Results

The ability of the observer to estimate the state a cube undergoing stationary, rotating, and translating motion was tested. For these classes of motion, the trajectory was further defined to assess the performance of the observer when 1,2 or 3 faces of the cube were visible to the sensor. Initial conditions and the scaling factors of the orientation, position and size update functions were defined to assess the individual and combined performance of these update functions. Key results of this analysis and an overall assessment of the observer's performance are presented in this section.

4.2.1 Orientation correction

4.2.1.1 Stationary Cube

When testing the orientation update alone, the position and size update functions were turned off by setting their scaling factors to 0. The initial size and position of the state estimate were assigned the ground truth values. The *angle error* between the predicted and ground truth orientation was computed to quantify performance. To compute this, the rotation matrix required to map the orientation of the predicted cube to that of the ground truth cube was computed over time. This was converted to the scaled-axis representation. The angle error was defined as the magnitude of this scaled-axis vector, representing the angular error between the predicted and ground truth orientation.

The results presented in Figure 4.9 are from trials where the cube was stationary and three faces were visible. Similar performance was achieved when two faces were visible. When no noise was present, the angle error quickly converged to 0. In fact, for the case of orientation correction alone, the observer guarantees global convergence. When noise was present, the error converged to the noise floor and exhibited a stable fluctuation about this limit. Given the mean and standard deviation of the Gaussian distributed range error, the angle error would be expected to cross 0 once the error converged to the noise floor. The reason this does not occur is due to small error in the orientation axis between the prediction and ground truth.

A limitation of the orientation update scheme was revealed when only a single cube face was visible to the sensor. The normals ($\hat{\mathbf{n}}$ and $\tilde{\mathbf{n}}$ in Figure 4.4) estimated from the predicted and

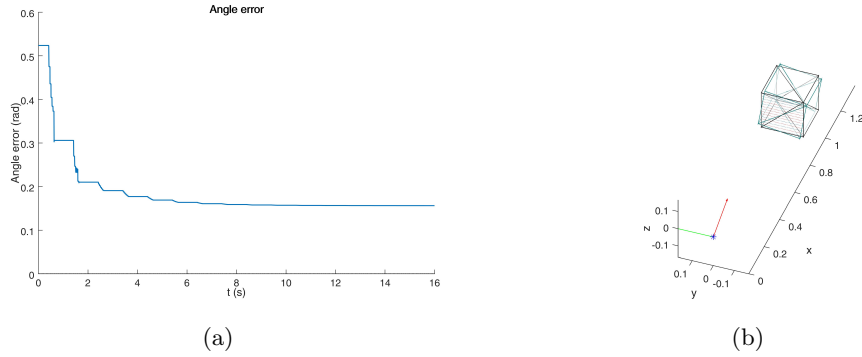


Figure 4.8: Orientation update when single cube face visible leads to (a) angle error, depicted in final state estimate (b).

measured intersection points were used to determine the rotation correction axis. However, this information is insufficient to correct for angular error about these normals themselves, as shown in Figure 4.8.

An approach considered to account for this was to apply a rotation to the predicted cube about the normal axis if the visibility pattern indicated by the set of indexes $\mathbf{u}(t)$ was not congruent for the prediction and measurement. This would effectively rotate the predicted cube until the faces aligned. However, this scheme was not used as it would later interfere with the performance of the orientation and size updates. Furthermore, it was unstable under noisy conditions and caused rotation away from the correct orientation. The recommendation for future work is to use the visibility pattern to estimate the actual rotation of the predicted and measured cubes about this normal axis before applying the necessary correction.

4.2.1.2 Moving Cube

Figure 4.10 shows the angular error for a trial where the ground truth cube rotated with an angular velocity of approximately 0.0327 rad/s such that 3 faces were visible to the sensor. The observer was given the ground truth initial orientation but an incorrect initial angular velocity of 0. Figure 4.10(a) shows that for noiseless measurements where orientation update is performed via the screw matrix, the observer is able to estimate the angular velocity of the cube and match its orientation. Again for noiseless measurements, Figure 4.10(b) shows that updating via the twist matrix initially provides a slower but smoother estimation of orientation. In trying to match the rotation of the cube, the angular velocity estimate overshoots the ground truth angular velocity and the angle error diverges. For

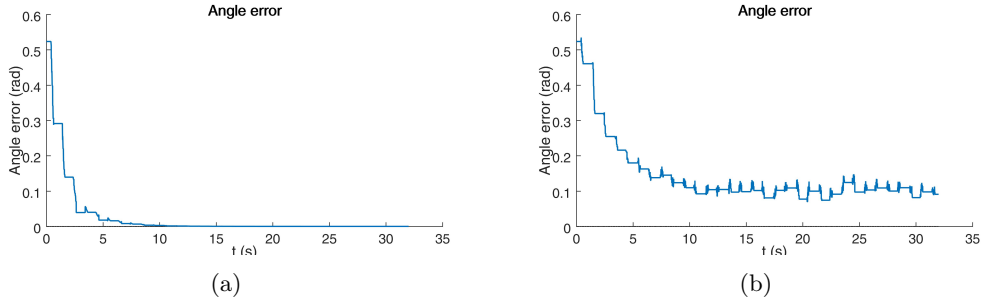


Figure 4.9: Angle error for (a) noiseless and (b) noisy measurements of stationary cube with 3 faces visible to sensor

noisy measurements, update via the screw in Figure 4.10(c) and twist in Figure 4.10(b) is unable to closely track the rotation of the cube. Updating via the twist matrix again results in overshoot.

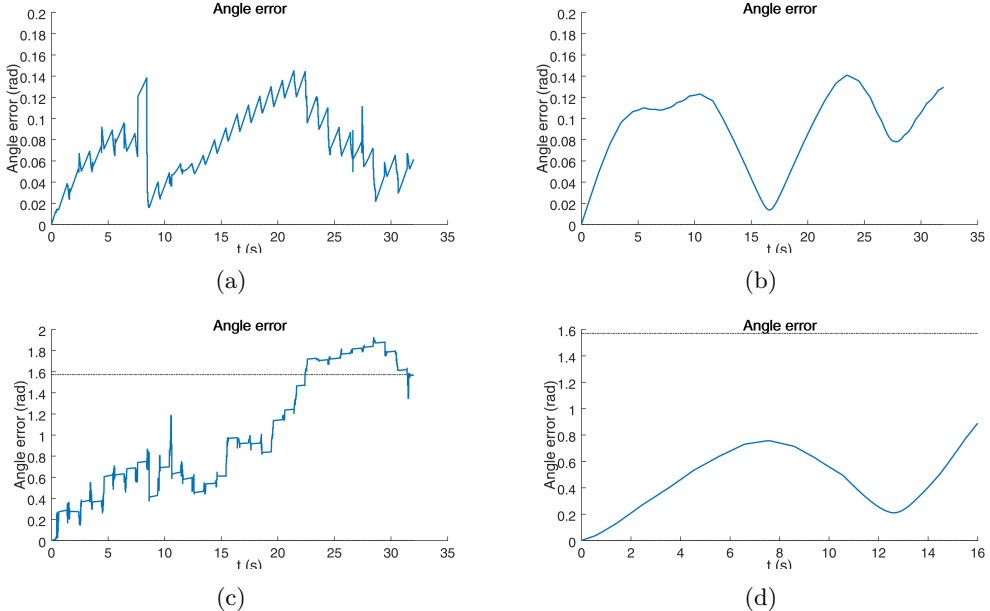


Figure 4.10: Angle error when cube rotating with angular velocity of approximately 0.0327 rad/s such that 3 faces visible to sensor. Noiseless measurements used to update orientation via (a) screw matrix and (b) twist matrix. Noisy measurements used to update orientation via (c) screw matrix and (d) twist matrix.

4.2.2 Position correction

Figure 4.11 shows the effect of the scale p_{scale} on the convergence behaviour of the position error. In these trials, one face of the cube was visible to the sensor. Figure 4.11(a) shows that for noiseless measurements, the position error converges to a region where it begins

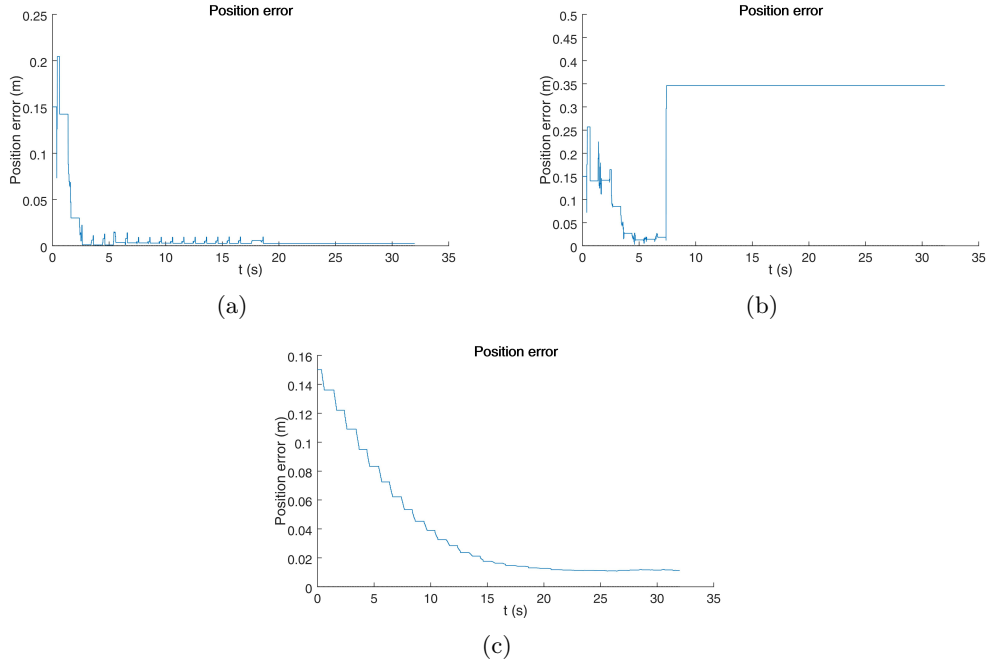


Figure 4.11: Position error for stationary cube with single face visible to sensor. Position error (a) converges quickly for noiseless measurements when $p_{scale} = 0.01$. Position error (b) is unstable for noisy measurements if $p_{scale} = 0.01$. Position error (c) converges to noise floor for noisy measurements when $p_{scale} = 0.001$.

to oscillate. Due to the dynamics of the scanning sensor, the size of the position update vector is too large and the estimate is unable to exactly align with the ground truth. Eventually, the estimate happens to align with the ground truth and the position error drops to 0.

Figure 4.11(b) shows that for noisy measurements, the update gain $p_{scale} = 0.01$ used in (a) is too large. A large random disturbance causes the position error to diverge so far that there is no longer any overlap between the estimated and ground truth cubes. At this point, no update can be computed. By reducing the gain to $p_{scale} = 0.001$, the position error for noisy measurements is able to converge slowly towards the noise floor.

In Figure 4.12, noiseless measurements are taken of a stationary cube with 2 faces visible to the sensor. Though the error shrinks slightly at first, the basin of attraction points away from the ground truth position. This occurs because the observer attempts to align the cube state estimate with the wrong face of the ground truth cube. The computed update vector will point in a direction orthogonal to the desired direction. The position update function is only successful when a single cube face is visible to the sensor. Future improvements should focus on designing a position update that is invariant to orientation.

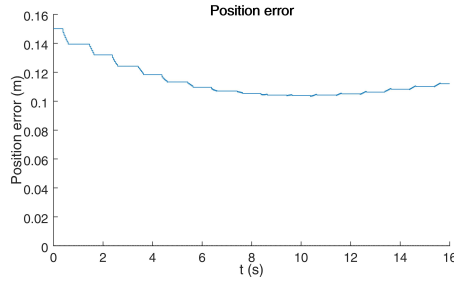


Figure 4.12: Position error for stationary cube with 2 faces visible to sensor

4.2.3 Size correction

The size correction function is extremely robust, able to globally converge to the noise floor regardless of the number of cube faces visible. Figure 4.13 shows that the *size error ratio* (the ratio between the size error and ground truth size) converges to 0 for noisy measurements of a stationary cube where 3 faces are visible to the sensor. In Figure 4.14, noisy measurements were taken of a cube rotating at 0.0327 rad/s and translating at 0.0094 m/s such that 3 faces were visible to the sensor. The ground truth twist was given as the initial twist estimate to allow the predicted cube to match the motion of the ground truth cube. In this case, the size error ratio still converged to the noise floor. The speed of the convergence suggests that the correction is dominated by case 2 of the size update function. This update scheme uses the mean range difference effectively measures the size difference. On the other hand, case 1 relies on the rarer occurrence of misaligned edges between the prediction and ground truth being observed to determine. However, case 1 will be required when there is non-zero position error, since a situation may arise where a combination of position and size error means that the predicted and ground truth cube faces lie the same distance from the sensor.

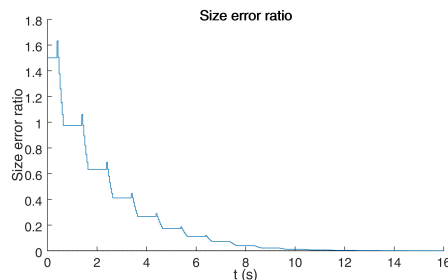


Figure 4.13: For noisy measurements of a stationary cube with 3 faces visible to the sensor, the size error ratio converges to the noise floor

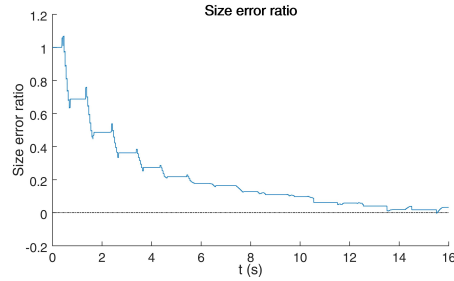


Figure 4.14: For noisy measurements of a cube rotating at 0.0327 rad/s and translating at 0.0094 m/s such that 3 faces are visible to the sensor, the size error ratio converges to the noise floor

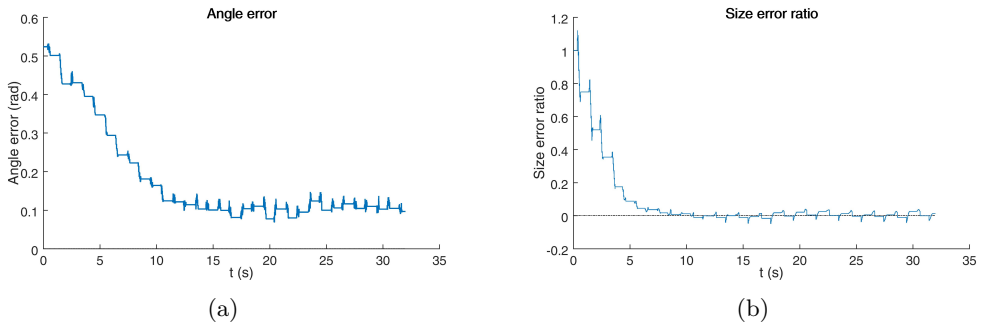


Figure 4.15: For noisy measurements of stationary cube with 3 faces visible to sensor, the angle error (a) and size error ratio (b) both converge to the noise floor.

4.2.4 Orientation and size correction

As the orientation and size update functions were effective individually, their ability to work simultaneously was tested.

For stationary cubes, the observer was able convergent for noiseless and noisy results, regardless of the number of cube faces visible to the sensor. Figure 4.15 shows the angle error and size error ratio converging to the noise floor for noisy measurements of a stationary cube where 3 faces were visible to the sensor.

A more systematic test was conducted with a wide range of initial conditions to verify this global convergence. Orientation and size correction were tested for initial angular error ranging from a minimum of 0 to a maximum of $\pi/4$ radians, and a minimum size error ratio of -0.5 to a maximum of 2. Noiseless range measurements were used. Figure 4.16 shows the time taken to converge to within 1% error. Comparing Figures 4.16(a) and 4.16(b) shows that the size error ratio always converges before the angle error. The magnitude of the initial angle error has little effect on the speed of the size error ratio

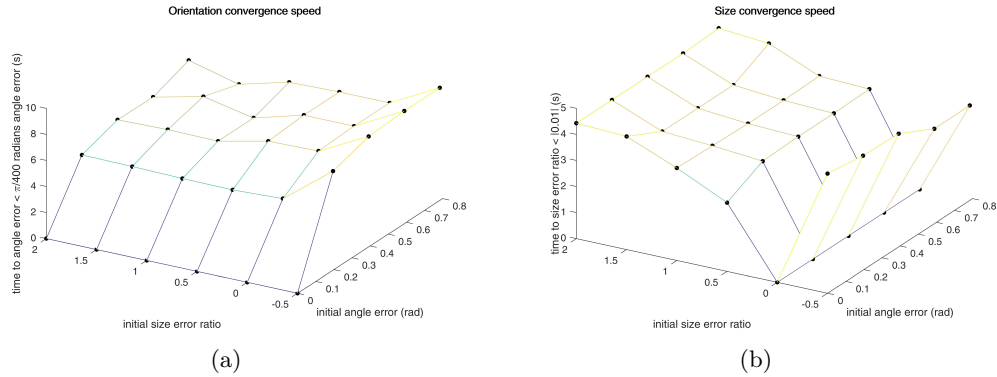


Figure 4.16: Time taken to converge to (a) angle error $< \pi/400$ radians (1% of maximum $\pi/4$ angle error) and (b) size error ratio $< |0.01|$ for range of initial conditions

convergence. The size correction only has a significant impact on the speed of orientation correction when the initial size estimate is smaller than the ground truth.

For noiseless measurements of a rotating cube, Figures 4.17(a) and 4.17(b) show that the observer is able to track the orientation of the cube when updating via the screw, and the size error ratio converges to the noise floor. Though the size error ratio in Figure 4.17(d) converges to the noise floor, Figure 4.17(c) shows that updating orientation via the twist results in overshoot. This also occurred when size correction was not being performed. Because the convergence of the size error ratio is so rapid, the performance of the observer when correcting both orientation and size is limited only by the effectiveness of the orientation update.

4.2.5 Discussion

ORIENTATION & SIZE GLOBALLY CONVERGENT

Add plot of convergence time for range of initial conditions. Equilibrium point - position error 0 - globally convergent. See what happens if position update turned on when position correct. does it still work? see what basin of attraction is. To make it globally convergent/larger basin of attraction - update must be invariant to $SO(3)$. Position update at the moment is not invariant to orientation. Orientation update seems to be invariant to position - explain this in detail.

The simulation results show that the size update is extremely robust. Given the correct position and orientation estimates, the size update function is globally convergent. For

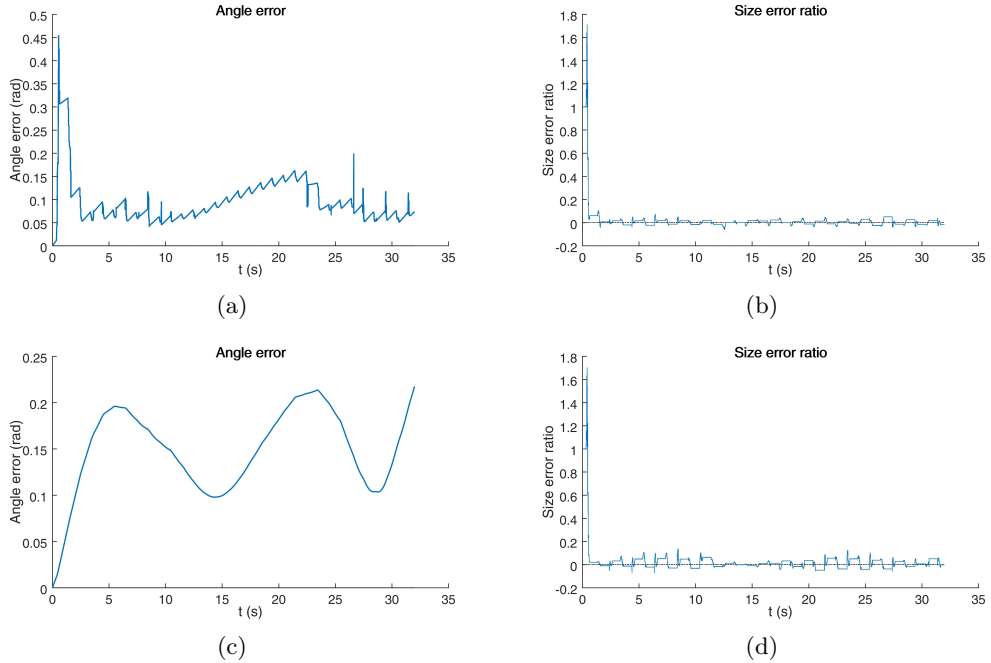


Figure 4.17: Noiseless measurements of cube rotating at 0.0327 rad/s such that 3 faces visible to sensor. Angle error (a) and size error ratio (b) when orientation updated via screw. Angle error (c) and size error ratio (d) when orientation updated via wrench.

the case of a stationary cube and correct size and position estimates, the orientation update function is also globally convergent though convergence is limited by the presence of noise. The symmetry of the cube means that the angle error is bounded to $\pi/4$ and the orientation correction converges quickly. The position update function was particularly unstable. Correction of the position error only converged for the special case where a single cube face was visible.

Another strength of the observer design is that it does not actually rely on the target object being a cube. Figure 4.18 shows that the orientation and size correction converges when the object to be estimated is a tetrahedron with side length $s = 0.5\text{m}$. The observer will likely give sensible results given that the target object is a platonic solid due to their symmetry.

These results show that the sparse measurements of a scanning sensor can be used to densely measure an infinite dimensional state.

Though updating the orientation via the twist gives a smoother estimation in comparison to the screw update, this results in overshoot. Initially, the angle error grows so the angular velocity increases to correct this. However, there is a delay in the response of the orientation

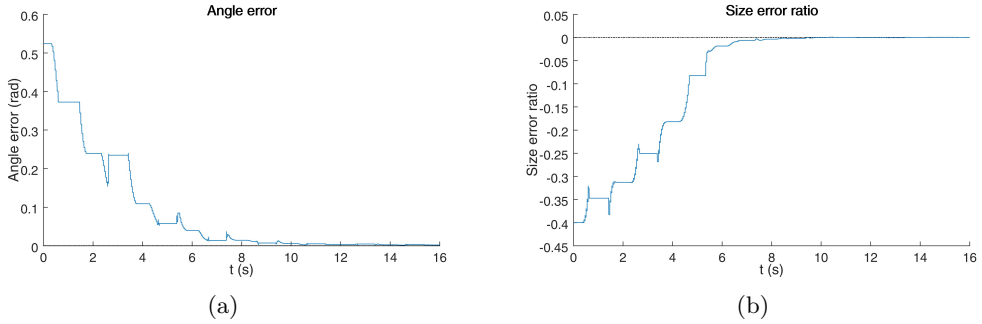


Figure 4.18: Angle error (a) and size error ratio (b) for noiseless measurements of tetrahedron of side length $s = 0.5\text{m}$

correction that causes the angular velocity to grow too large. The overcompensation then occurs in the other direction and the error diverges. In control theory, this problem is solved with *feed-forward control* which anticipates overshoot and corrects for it before it can occur. A topic of future research would be to investigate if an observer analogue to feed-forward control exists. A possible starting point could be to investigate applying combinations of screw and twist updates that combine the responsiveness of the screw update and the smoothness of the twist update.

These simulated results showed that the size and orientation update functions in this initial observer implementation show promise. To improve performance, a more robust position update function must be designed. A possible approach would be to augment the cube state with a measure of the centre of mass of a history of measured points. Over time, the difference in the estimate and measurement of this variable would produce a more accurate position update vector.

Once a working position update function is implemented, the next step is to combine the position and orientation update functions. Such a function would act on the screw, twist or wrench, rather than correcting only the linear or angular terms. Designing this innovation function to be invariant under actions of $\mathbf{SE}(3)$ will result in improved global convergence properties.

A symmetry preserving observer would allow design methods for linear, infinite dimensional observers to be utilised. This would allow the environment to be represented as infinite dimensional state. The observer would not need to separate the target object and the background. Instead, an estimate of the entire depth field could be computed.

Chapter 5

Experimental Data

In order to validate the performance of the observer implementation, experimental data was collected with a Hokuyo UBG-04LX-F01 scanning laser range-finder.

Measurements were taken to:

- build a model of the noise characteristics of the Hokuyo UBG-04LX-F01 in order to more accurately simulate the performance of the observer;
- observe the motion of a moving cube of known state to test the observer in real-world conditions.

Section 5.1 details how measurements were taken to develop the noise model. Section 5.2 describes how experimental range measurements were taken and how the ground truth cube state was determined. This work is still ongoing as the data must be calibrated before it can be used to assess the performance of the observer.

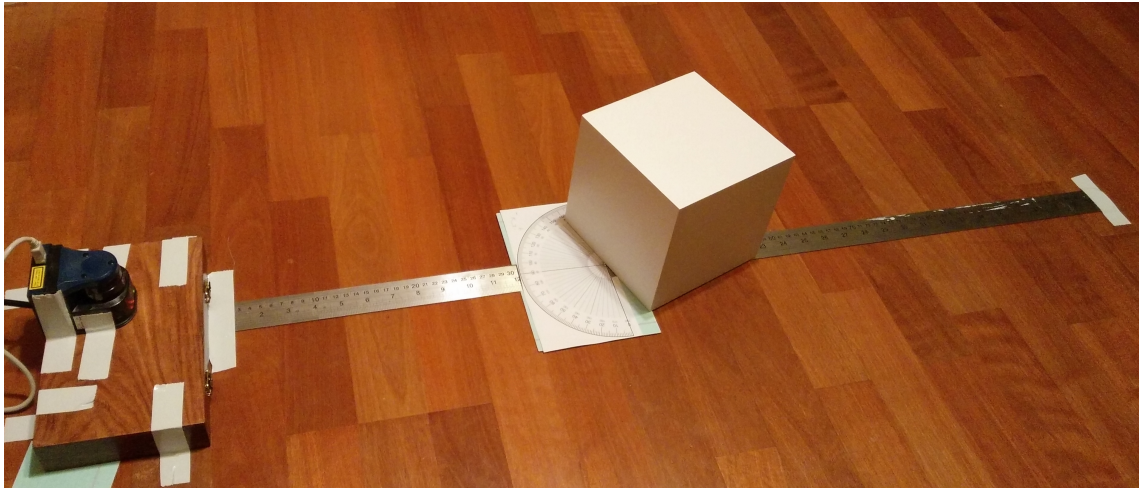


Figure 5.1: setup to measure noise at a different ranges and angle (lights turned off during measurement to eliminate error from variation in lighting conditions)

5.1 Sensor Noise Characterisation

An accurate range sensor simulation must include a model for the error distribution of the measurements. A noise model for the Hokuyo UBG-04LX-F01 used in this research was developed in by Park et al. [25]. The effect of range and incidence angles on the error was measured, but a unified model combining both was not provided. Furthermore, [25] showed that the measurement error depends highly on the texture and colour of the surface measured. To accurately model the Hokuyo UBG-04LX-F01 for the usage case of this research, a wide range of measurements using a specific surface were taken to determine the effect of range and incidence angle on the error distribution.

5.1.1 Measurement Setup

A flat surface was painted matte white. The surface was placed perpendicular to the ground and at a known distance and angle with respect to the range sensor. 1200 samples of the measured distance to the surface were taken.

For this research, the cube is likely to be placed within 1.5m from the sensor and at any orientation. The range error distribution for these conditions should be measured. The distance from the sensor to the measurement surface was thus varied in 50mm increments between 250mm and 1750mm, to an accuracy of $\pm 1\text{mm}$. At each of these ranges the incidence angles was varied in 20° increments from 0° to 80° to an accuracy of $\pm 0.5^\circ$. The physical setup is shown in Figure 5.1.

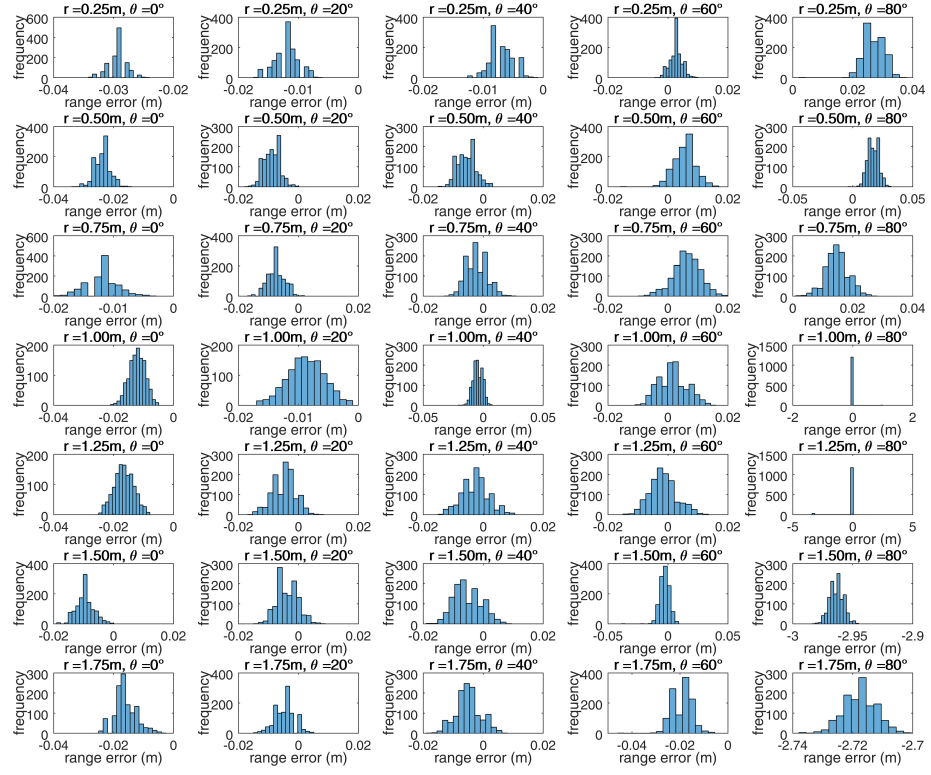


Figure 5.2: Sensor noise function $f_{UBG}(r, \theta)$ approximately normally distributed

5.1.2 Results

The range error $r_{error} = r_{groundtruth} - r_{measured}$ was computed. The distributions of this error for varying ranges and angles is shown in Figure 5.2. The range error is approximately normally distributed.

The mean range error as function of r and θ is shown in Figure 5.3. The standard deviation of the range errors as function of r and θ is shown in Figure 5.4.

Figures 5.3(a) and 5.4(a) show that the mean error and error standard deviation increase significantly when $\theta > 75^\circ$ and $r > 0.8m$. This can be explained by considering what happens to the laser beam under these conditions. Though it has been idealised as a ray in the simulation, the laser has a nonzero beam width. Thus, as θ increases, one side of the beam will encounter the surface before the centre of the beam. A portion of the light will reach the sensor earlier, though the total amount of light will be reduced as the angle increases. This earlier reflected light will result in a shorter range measurement, but less reflected light will cause a longer range measurement. For angles greater than 75° and

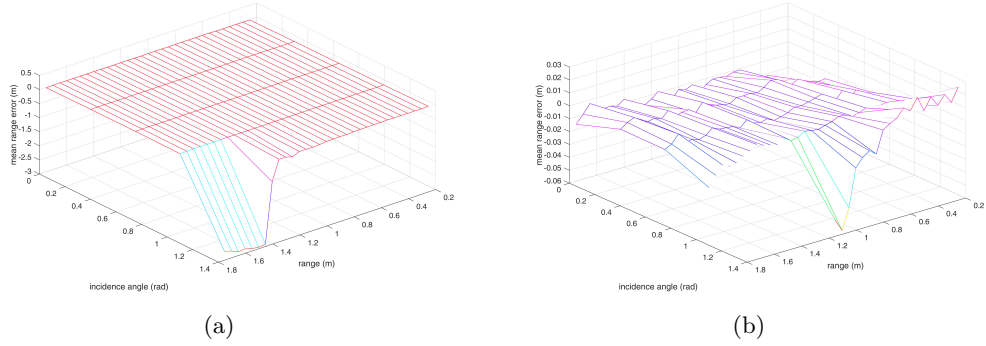


Figure 5.3: mean range error ($r_{error} = r_{groundtruth} - r_{measured}$) vs (r, θ) showing (a) large error at high angles and range, (b) overall shape

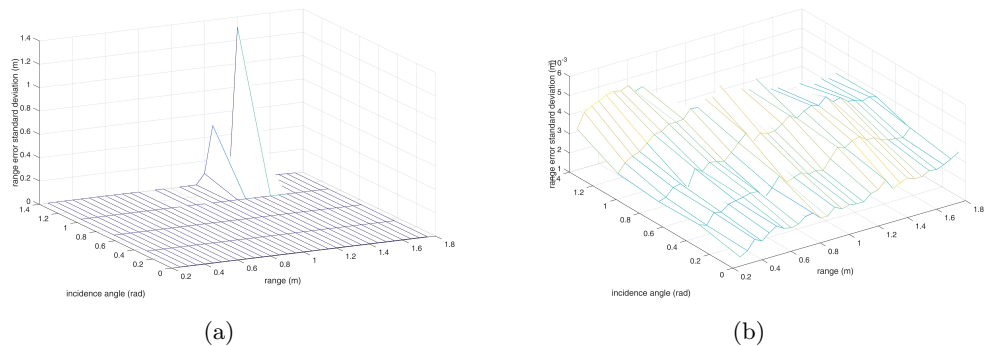


Figure 5.4: range error σ vs (r, θ) showing (a) outliers/large std dev at high angles and range, (b) overall shape

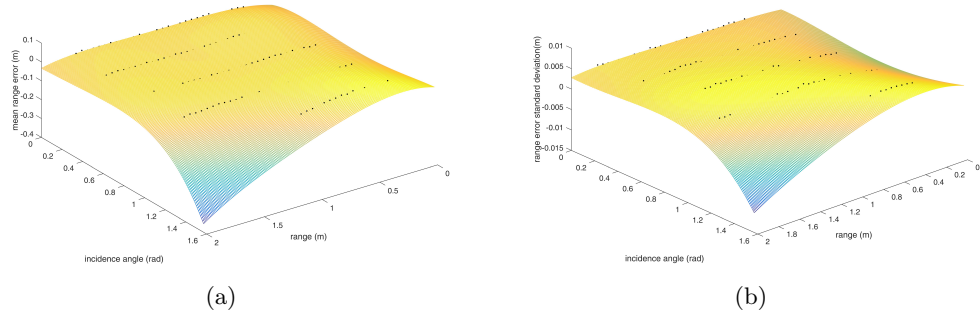


Figure 5.5: polynomials fitted to range error mean & standard deviation data points to model noise. (a) SSE: 0.003234, R-square: 0.8447, Adjusted R-square: 0.8278, RMSE: 0.005027(b) SSE: 7.592e-06, R-square: 0.9196, Adjusted R-square: 0.9103, RMSE: 0.0002515

ranges greater than 0.8m, the reflected light is insufficient to allow a range measurement. The sensor returns the maximum possible range measurement of 4095mm. In modelling the noise, range measurements for $\theta > 75^\circ$ and $r > 0.8\text{m}$ are discarded.

These results are corroborated by [25] who reported difficulty in acquiring measurements for high angles and modelled the noise distribution as Gaussian.

DISCUSS: does scan direction make a difference? future tests should see if $-\theta$ same as θ

4th degree polynomial surfaces in equations 5.2 and 5.3 were fitted to the adjusted set of data points using Matlab's curve fitting tool. The surfaces and the goodness of fit are shown in Figure 5.5.

5.1.2.1 Gaussian noise model

$$\tilde{r}(r, \theta) = \begin{cases} f_s(r, \theta, \phi(k)) = r + \mathcal{N}(\mu, \sigma) & \theta \leq 75^\circ \text{ or } r \leq 0.8 \\ NaN & \theta > 75^\circ \text{ and } r > 0.8 \end{cases} \quad (5.1)$$

where

$$\begin{aligned}\mu = & a_{00} + a_{10}r + a_{01}\theta + a_{20}r^2 + a_{11}r\theta + a_{02}\theta^2 \\ & + a_{30}r^3 + a_{21}r^2\theta + a_{12}r\theta^2 + a_{03}\theta^3 + a_{40}r^4 \\ & + a_{31}r^3\theta + a_{22}r^2\theta^2 + a_{13}r\theta^3 + a_{04}\theta^4\end{aligned}\quad (5.2)$$

$$\begin{aligned}
\sigma = & b_{00} + b_{10}r + b_{01}\theta + b_{20}r^2 + b_{11}r\theta + b_{02}\theta^2 \\
& + b_{30}r^3 + b_{21}r^2\theta + b_{12}r\theta^2 + b_{03}\theta^3 + a_{40}r^4 \\
& + b_{31}r^3\theta + b_{22}r^2\theta^2 + b_{13}r\theta^3 + b_{04}\theta^4
\end{aligned} \tag{5.3}$$

and coefficients a_{ij} and b_{ij} are provided in tables 5.1 and 5.2 respectively.

Table 5.1: a_{ij} coefficients

	j_0	j_1	j_2	j_3	j_4
i_0	-0.06529	0.2126	-0.533	0.4629	-0.1223
i_1	0.2024	-0.1906	0.4006	-0.1791	0
i_2	-0.3074	0.0228	-0.0716	0	0
i_3	0.2053	0.01455	0	0	0
i_4	-0.04912	0	0	0	0

Table 5.2: b_{ij} coefficients

	j_0	j_1	j_2	j_3	j_4
i_0	0.001242	0.2126	-0.01128	0.01162	-0.002746
i_1	0.00352	0.006146	0.01021	-0.007316	0
i_2	-0.005138	-0.00626	-0.0005068	0	0
i_3	0.004067	0.001337	0	0	0
i_4	-0.001092	0	0	0	0

5.1.2.2 Surface noise

An additional source of error was observed and found to be mostly independent of r and θ . This may be caused by surface properties of the environment, though the error is larger than expected in this case. A possible explanation is compensation performed by sensor to produce globally straight lines. While flat surfaces do appear flat from a distance, locally there are regular variations in depth as shown in Figure 5.6(a).

This surface noise was modelled with a random walk function

$$e_{surface} = a \sum_{n=1}^{n_{Steps}} -1 + 2 \lfloor \mathcal{R} \rfloor \tag{5.4}$$

where \mathcal{R} is a random variable following a uniform distribution on $[0,1]$. A step size $a = 0.0005m$ was used. Figure 5.6 shows that this model accurately models the measured surface variations. It should be noted that the measured variation appears concave while the simulated noise appears convex. This is due to the nature of the random walk noise.

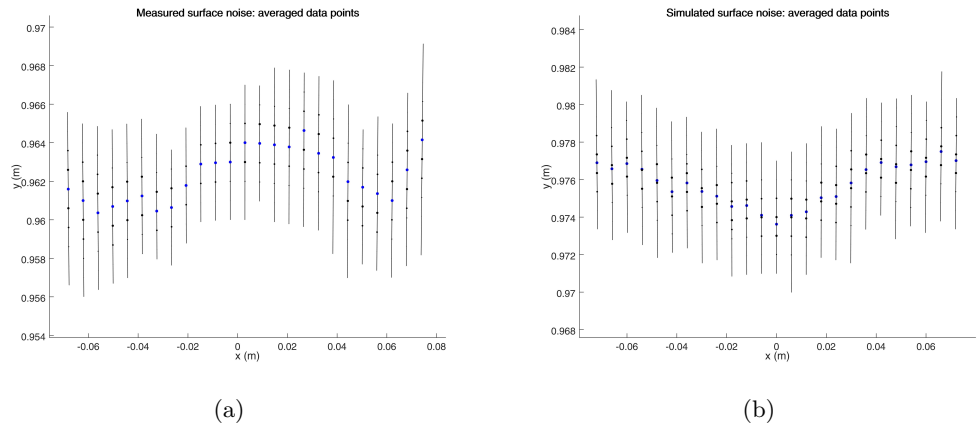


Figure 5.6: Comparision of (a) measured and (b) simulated surface noise. Point distribution along radial lines is shown as quintiles of error.

Over a large sample, both concave and convex surface noise is observed in real-world measurements and the simulate random walk simulation.



Figure 5.7: setup to collect experimental data

5.2 Observer Performance Testing Data

Data collected to assess the performance of the observer under real-world, less-than-ideal conditions.

5.2.1 Setup

The experimental setup is shown in Figure 5.7.

The Hokuyo UBG-04LX-F01 sensor was mounted to a tripod. The sensor was panned up and down manually while the range and time recorded. This panning along with its own scanning behaviour allows the sensor to densely measure the infinite-dimensional environment depth field. To compute the elevation angle of the sensor, the range measurements to a portion of the blank wall were used. The range to this wall was measured at elevations increasing from -25° to 25° in 5° increments for calibration purposes.

The target object was a cube of 100mm side length cube made from medium-density

fibreboard. The cube was spray painted matte white - the same surface as used in the sensor noise modelling in Section 5.1.

The cube was placed in the gripper of a Kinova Jaco robotic arm. The arm was manually manipulated to produce stationary, rotating, translating and combined motions. The joint angles of the sensor over time were recorded. From this data, the forward kinematic model for the arm was used to compute the ground truth pose of the cube over time.

5.2.2 Results

Calibration of the data to determine the elevation angle of the sensor is yet to be completed. However, it is unlikely that the current implementation of the observer will be able to estimate the cube state from this data. Because the cube is held by the gripper of the arm, neither the range or continuity assumptions in Section 4.1.5.2 hold.

An infinite-dimensional observer measuring the entire depth field would give a better estimate of the state of the cube. A symmetry-preserving observer would likely be more robust to the significant levels of noise in the data set.

Conclusion

refer back to context, literature, motivation

implemented observer - dense sensor.

results promising - dense sensor capable of observing infinite dimensional system

implementation reveals limitations of finite dimensional, non-invariant design method -
position and orientation don't work well together

shows that new research into invariant design is promising avenue of research, clear ways
to solve problems encountered with this implementation

Bibliography

- [1] P. Stavroulakis and P. Sarachik, “Design of optimal controllers for distributed systems using finite dimensional state observers,” in *Decision and Control including the 12th Symposium on Adaptive Processes, 1973 IEEE Conference on.* IEEE, 1973, pp. 105–109.
- [2] L. Meirovitch and H. Baruh, “On the problem of observation spillover in self-adjoint distributed-parameter systems,” *Journal of Optimization Theory and Applications*, vol. 39, no. 2, pp. 269–291, 1983.
- [3] C. Harkort and J. Deutscher, “Finite-dimensional observer-based control of linear distributed parameter systems using cascaded output observers,” *International Journal of Control*, vol. 84, no. 1, pp. 107–122, 2011.
- [4] R. V. Gressang and G. B. Lamont, “Observers for systems characterized by semigroups,” *Automatic Control, IEEE Transactions on*, vol. 20, no. 4, pp. 523–528, 1975.
- [5] A. Smyshlyaev and M. Krstic, “Backstepping observers for a class of parabolic pdes,” *Systems & Control Letters*, vol. 54, no. 7, pp. 613–625, 2005.
- [6] K. Ramdani, M. Tucsnak, and G. Weiss, “Recovering the initial state of an infinite-dimensional system using observers,” *Automatica*, vol. 46, no. 10, pp. 1616–1625, 2010.
- [7] G. Haine, “Recovering the observable part of the initial data of an infinite-dimensional linear system with skew-adjoint generator,” *Mathematics of Control, Signals, and Systems*, vol. 26, no. 3, pp. 435–462, 2014.
- [8] J. Primbs, “Survey of nonlinear observer design techniques,” 1996.

- [9] C.-Z. Xu, P. Ligarius, and J.-P. Gauthier, “An observer for infinite-dimensional dissipative bilinear systems,” *Computers & Mathematics with Applications*, vol. 29, no. 7, pp. 13–21, 1995.
- [10] H. Bounit and H. Hammouri, “Observers for infinite dimensional bilinear systems,” *European journal of control*, vol. 3, no. 4, pp. 325–339, 1997.
- [11] S. I. Marcus, “Algebraic and geometric methods in nonlinear filtering,” *SIAM Journal on Control and Optimization*, vol. 22, no. 6, pp. 817–844, 1984.
- [12] S. Salcudean, “A globally convergent angular velocity observer for rigid body motion,” *Automatic Control, IEEE Transactions on*, vol. 36, no. 12, pp. 1493–1497, 1991.
- [13] N. Aghannan and P. Rouchon, “On invariant asymptotic observers,” in *Decision and Control, 2002, Proceedings of the 41st IEEE Conference on*, vol. 2. IEEE, 2002, pp. 1479–1484.
- [14] D. S. Maithripala, W. P. Dayawansa, and J. M. Berg, “Intrinsic observer-based stabilization for simple mechanical systems on lie groups,” *SIAM journal on control and optimization*, vol. 44, no. 5, pp. 1691–1711, 2005.
- [15] S. Bonnabel and P. Rouchon, “On invariant observers,” in *Control and observer design for nonlinear finite and infinite dimensional systems*. Springer, 2005, pp. 53–65.
- [16] S. Bonnabel, P. Martin, and P. Rouchon, “Symmetry-preserving observers,” *Automatic Control, IEEE Transactions on*, vol. 53, no. 11, pp. 2514–2526, 2008.
- [17] ——, “Non-linear symmetry-preserving observers on lie groups,” *Automatic Control, IEEE Transactions on*, vol. 54, no. 7, pp. 1709–1713, 2009.
- [18] D. Auroux and S. Bonnabel, “Symmetry-based observers for some water-tank problems,” *Automatic Control, IEEE Transactions on*, vol. 56, no. 5, pp. 1046–1058, 2011.
- [19] R. Mahony, T. Hamel, J. Trumpf, and C. Lageman, “Nonlinear attitude observers on so (3) for complementary and compatible measurements: A theoretical study,” in *Decision and Control, 2009 held jointly with the 2009 28th Chinese Control Conference. CDC/CCC 2009. Proceedings of the 48th IEEE Conference on*. IEEE, 2009, pp. 6407–6412.

- [20] J. Trumpf, R. Mahony, T. Hamel, and C. Lageman, “Analysis of non-linear attitude observers for time-varying reference measurements,” *Automatic Control, IEEE Transactions on*, vol. 57, no. 11, pp. 2789–2800, 2012.
- [21] R. Mahony, J. Trumpf, and T. Hamel, “Observers for kinematic systems with symmetry,” in *Proceedings of the 9th IFAC symposium on nonlinear control systems*, vol. 9, 2013, pp. 617–633.
- [22] N. Zarrouati-Vissière, “Augmented reality: the fusion of vision and navigation,” Ph.D. dissertation, Ecole Nationale Supérieure des Mines de Paris, 2013.
- [23] J. D. Adarve, D. J. Austin, and R. Mahony, “A filtering approach for computation of real-time dense optical-flow for robotic applications.”
- [24] D. G. Luenberger, “Observers for multivariable systems,” *Automatic Control, IEEE Transactions on*, vol. 11, no. 2, pp. 190–197, 1966.
- [25] C.-S. Park, D. Kim, B.-J. You, and S.-R. Oh, “Characterization of the hokuyo ubg-04lx-f01 2d laser rangefinder,” in *RO-MAN, 2010 IEEE*. IEEE, 2010, pp. 385–390.